Reconstruction of Polarization Properties of Whistler Waves From Two Magnetic and Two Electric Field Components: Application to Parker Solar Probe Measurements

L. Colomban, O. V. Agapitov, V. Krasnoselskikh, Matthieu Kretzschmar, Thierry Dudok de Wit, S. Karbashewski, F. S. Mozer, J. W. Bonnell, S. Bale, D. Malaspina, et al.

JGR Space Physics

METHOD
10.1029/2023JA031427

Reconstruction of Polarization Properties of Whistler Waves From Two Magnetic and Two Electric Field Components: Application to Parker Solar Probe Measurements

L. Colomban[1], O. V. Agapitov[2,3], V. Krasnoselskikh[1,2], M. Kretzschmar[1], T. Dudok de Wit[1,4], S. Karbashewski[2], F. S. Mozer[2], J. W. Bonnell[2], S. Bale[2,5], D. Malaspina[6,7], and N. E. Raouafi[8]

[1]LPC2E, CNRS/University of Orléans/CNES, 3A avenue de la Recherche Scientifique, Orléans, France, [2]Space Sciences Laboratory, University of California, Berkeley, CA, USA, [3]Astronomy and Space Physics Department, National Taras Shevchenko University of Kyiv, Kyiv, Ukraine, [4]International Space Science Institute, ISSI, Bern, Switzerland, [5]Physics Department, University of California, Berkeley, CA, USA, [6]Laboratory for Atmospheric and Space Physics, University of Colorado, Boulder, CO, USA, [7]Astrophysical and Planetary Sciences Department, University of Colorado, Boulder, CO, USA, [8]Applied Physics Laboratory, Johns Hopkins University, Laurel, MD, USA

Abstract The search-coil magnetometer (SCM) aboard Parker Solar Probe (PSP) measures the 3 Hz to 1 MHz magnetic field fluctuations. During Encounter 1, the SCM operated as expected; however, in March 2019, technical issues limited subsequent encounters to two components for frequencies below 1 kHz. Detrimentally, most whistler waves are observed in the affected frequency band where established techniques cannot extract the wave polarization properties under these conditions. Fortunately, the Electric Field Instrument aboard PSP measures two electric field components and covers the affected bandwidth. We propose a technique using the available electromagnetic fields to reconstruct the missing components by neglecting the electric field parallel to the background magnetic field. This technique is applicable with the assumptions of (a) low-frequency whistlers in the plasma frame relative to the electron cyclotron frequency; (b) a small propagation angle with respect to the background magnetic field; and (c) a large wave phase speed relative to the cross-field solar wind velocity. Critically, the method cannot be applied if the background magnetic field is aligned with the affected SCM coil. We have validated our method using burst mode measurements made before March 2019. The reconstruction conditions are satisfied for 80% of the burst mode whistlers detected during Encounter 1. We apply the method to determine the polarization of a whistler event observed after March 2019 during Encounter 2. Our novel method is an encouraging step toward analyzing whistler properties in affected encounters and improving our understanding of wave-particle interactions in the young solar wind.

Key Points:

- We present a method to determine whistler wave polarization without a magnetic field component (Parker Solar Probe regime after March 2019)
- This allows us to expand whistler wave statistical databases; this is an essential step to better understanding wave-particle interactions
- We demonstrate that this method applies to 80% of whistler waves observed in burst-mode data from the first encounter

Correspondence to:
L. Colomban,
lucas.colomban@cnrs-orleans.fr

Citation:
Colomban, L., Agapitov, O. V., Krasnoselskikh, V., Kretzschmar, M., Dudok de Wit, T., Karbashewski, S., et al. (2023). Reconstruction of polarization properties of whistler waves from two magnetic and two electric field components: Application to Parker Solar Probe measurements. *Journal of Geophysical Research: Space Physics*, *128*, e2023JA031427. https://doi.org/10.1029/2023JA031427

Received 20 FEB 2023
Accepted 8 SEP 2023

Author Contributions:
Conceptualization: L. Colomban, O. V. Agapitov, V. Krasnoselskikh, M. Kretzschmar
Data curation: S. Karbashewski
Formal analysis: L. Colomban, O. V. Agapitov
Funding acquisition: O. V. Agapitov, V. Krasnoselskikh, M. Kretzschmar
Methodology: L. Colomban, O. V. Agapitov, V. Krasnoselskikh, M. Kretzschmar, T. Dudok de Wit, F. S. Mozer, J. W. Bonnell, S. Bale, D. Malaspina, N. E. Raouafi
Supervision: O. V. Agapitov, V. Krasnoselskikh, M. Kretzschmar

1. Introduction

Parker Solar Probe (PSP) was launched in August 2018 to collect measurements of plasma parameters and electromagnetic fields in the inner heliosphere below 50 solar radii ($R_\odot$) offering unique opportunities to study in situ the young solar wind (Bale et al., 2019; Fox et al., 2016; Howard et al., 2019; Kasper et al., 2019; McComas et al., 2019; Raouafi et al., 2023). The first solar encounter had its perihelion at 35.7 $R_\odot$; subsequent perihelia over the 7-year mission will drop closer to the Sun, eventually reaching a heliocentric distance of about 10 $R_\odot$ in mid-2025. The mission addresses two fundamental problems in space physics: coronal plasma heating and the acceleration of solar wind plasmas. In both problems, wave-particle interactions involving magnetohydrodynamic (MHD) and kinetic-scale waves are known to play an important role; one of the widely studied waves in the latter category is the whistler wave.

Whistlers are right-hand polarized electromagnetic modes observed between the lower hybrid frequency (f_{lh}) and electron cyclotron frequency f_{ce} (Chust et al., 2021; Gurnett & Anderson, 1977; Kretzschmar et al., 2021; Lacombe et al., 2014; Neubauer et al., 1977). Common whistler generation mechanisms are heat flux instability (Gary et al., 1975; López et al., 2019; Tong, Vasko, Pulupa, et al., 2019), fan instability (Bošková et al., 1992; Kadomtsev & Pogutse, 1968; Krafft & Volokitin, 2003; Vasko et al., 2019; Verscharen et al., 2019), temperature anisotropy instability (Jagarlamudi et al., 2020; Lazar et al., 2011, 2013, 2018; Sagdeev & Shafranov, 1960; Vasko et al., 2020), and electron populations trapped in magnetic field inhomogeneities (Agapitov et al., 2020; Karbashewski et al., 2023) often associated with boundaries of localized magnetic field deflections that are

Validation: L. Colomban, O. V. Agapitov, V. Krasnoselskikh, M. Kretzschmar, T. Dudok de Wit
Visualization: L. Colomban, O. V. Agapitov, V. Krasnoselskikh, M. Kretzschmar
Writing – original draft: L. Colomban, O. V. Agapitov, V. Krasnoselskikh, M. Kretzschmar, T. Dudok de Wit, S. Karbashewski, F. S. Mozer, J. W. Bonnell, S. Bale, D. Malaspina, N. E. Raouafi
Writing – review & editing: L. Colomban, O. V. Agapitov, V. Krasnoselskikh, M. Kretzschmar, T. Dudok de Wit, S. Karbashewski, F. S. Mozer, J. W. Bonnell, S. Bale, D. Malaspina, N. E. Raouafi

called switchbacks (Agapitov et al., 2022; Bale et al., 2019; Dudok de Wit et al., 2020; Kasper et al., 2019; Krasnoselskikh et al., 2020). These waves have been studied by several missions, such as Helios (Jagarlamudi et al., 2020), Cluster (Lacombe et al., 2014), Artemis (Stansby et al., 2016; Tong, Vasko, Artemyev, et al., 2019), Solar Orbiter (Chust et al., 2021; Kretzschmar et al., 2021), STEREO (Breneman et al., 2010; Cattell et al., 2020) and PSP (Agapitov et al., 2020; Cattell et al., 2020, 2021, 2022; Dudok de Wit et al., 2022; Froment et al., 2023; Jagarlamudi et al., 2021; Karbashewski et al., 2023). As more observations are made about the dynamics of the solar wind, whistler waves have emerged as a strong candidate for interacting efficiently with solar wind electron populations (Gary & Feldman, 1977; Gary et al., 1975, 1999; Kajdič et al., 2016; Scime et al., 1994; Vocks & Mann, 2003).

Electrons in the solar wind are accurately described by three distinct populations: a bulk thermal component with close to Maxwellian distributions and two suprathermal fractions called the Strahl and halo. The halo population is quasi-isotropic (Feldman et al., 1975, 1978; Lazar et al., 2020) and is often represented by Kappa distributions (Lazar et al., 2015; Maksimovic et al., 1997; Scudder, 1992a, 1992b). The Strahl is a beam of high-energy electrons that follows the magnetic field lines, propagating away from the Sun (Pilipp et al., 1987; Rosenbauer et al., 1976, 1977). The relative proportions of the two suprathermal populations are observed to evolve with radial distance from the Sun. Notably, the fractional density of halo electrons increases with distance while the Strahl distribution broadens (Bercic et al., 2019; Graham et al., 2017; Hammond et al., 1996) and its fractional density decreases with distance (Graham et al., 2017; Halekas et al., 2020, 2021; Maksimovic et al., 2005; Štverák et al., 2009). These observations suggest there are mechanisms, such as wave-particle interactions involving whistler waves, responsible for scattering the beam-like Strahl electrons into a more isotropic halo distribution. Several polarization properties determine the efficiency of whistler wave interactions with the Strahl and halo suprathermal electron populations. For example, two important parameters are the direction of propagation with respect to the Sun (i.e., sunward or anti-sunward propagation), and the wave normal angle (WNA), θ, which is the angle between the wave vector, $\mathbf{k}$, and the background magnetic field, $\mathbf{B_0}$. Sunward propagating whistlers scatter the Strahl population in the pitch-angle space more efficiently (up to two orders of magnitude greater) than the anti-sunward propagating waves (Cattell & Vo, 2021; Saito & Gary, 2007; Sarfraz & Yoon, 2020; Vocks et al., 2005). The situation becomes more complicated if anti-sunward whistler waves have high WNA and thus provide efficient scattering (Artemyev et al., 2013, 2016; Cattell & Vo, 2021; Cattell et al., 2022; Micera et al., 2020, 2021; Roberg-Clark et al., 2019; Vasko et al., 2019). This makes the polarization properties of whistler waves observed by PSP one of the key factors for the quantification of the wave-particle interaction effects in the solar wind.

To date, a wide array of whistler observations made by PSP have been reported on. In previous studies, the polarization properties of whistler waves in the young solar wind were inferred from the three search-coil magnetometer (SCM) components during Encounter 1 (Agapitov et al., 2020; Cattell et al., 2020, 2021, 2022; Dudok de Wit et al., 2022; Froment et al., 2023; Karbashewski et al., 2023). The statistical study of whistler properties by Froment et al. (2023) revealed that most of the whistler wave packets recorded during Encounter 1 were quasi-parallel to the background magnetic field: 97% had WNA between 0 and 25°. Whistler waves were observed in the frequency range from the local lower hybrid frequency f_{lh} up to $0.2f_{ce}$. The observed oblique whistlers (with WNA >45°) tend to have lower frequencies than the quasi-parallel whistlers. The sunward propagating whistler waves, both quasi-parallel and oblique waves, were often collocated with short-lived magnetic dips observed at switchback boundaries; this indicates a possible generation of whistlers in these structures (Agapitov et al., 2020; Froment et al., 2023; Karbashewski et al., 2023). These waves tend to be detected at frequencies that are lower than those for waves that are not collocated with magnetic dips (Froment et al., 2023). Another statistical study by Cattell et al. (2022), on the basis of electric field measurements from the first nine encounters, showed that below the heliocentric distance of 100 $R_\odot$ whistler wave frequencies in the spacecraft frame were below $0.2f_{ce}$ with the tendency to decrease below $0.1f_{ce}$ when approaching the Sun closer than 50 $R_\odot$. To further elucidate the impact of whistler waves on the suprathermal electrons it is necessary to extend the statistics reported by Froment et al. (2023) for Encounter 1 (the only one available with a full set of SCM magnetic measurements (Dudok de Wit et al., 2022)) to the later encounters and update the statistics of whistler waves presented by Cattell et al. (2021, 2022) with the wave polarization parameters.

A change in the response in one of the SCM components: $B\mathrm{w}_\mathrm{u}$ of the SCM reference frame, (**u**, **v**, **w**) (Malaspina et al., 2016), appeared after March 2019. Here and in the following $\vec{B}\mathrm{w}$ and $\vec{E}\mathrm{w}$ represent the wave magnetic and electric perturbations, respectively. This anomaly considerably reduces the amplitude of the $B\mathrm{w}_\mathrm{u}$ component in

the frequency range of whistler waves (typically, below 400 Hz) and also affects its phase. This makes it impossible to unambiguously determine the polarization properties using the three components of the magnetic field and the two components of the electric field. The inability to determine the whistler wave properties beyond Encounter 1 has motivated us to propose a novel technique for reconstructing the whistler wave polarization parameters. The technique uses the two components of the SCM that are available together with the two electric field components recorded by the Electric Field Instrument (EFI). It can be noted that the STEREO spacecraft have electrical antennas that measure three components of the electric field but do not have SCMs. Breneman et al. (2010) therefore developed a method based on the whistler wave cold dispersion relation and the ratio of transverse electric field components to determine whistler WNAs. This method is not designed to reconstruct electromagnetic field components and is different from the one proposed here. In addition, in the case of Breneman et al. (2010) the absence of magnetic field fluctutaions measurements makes it impossible to determine the direction of propagation.

In the following, we present the data used (Section 2.1), our reconstruction method (Section 2.2) and its range of applicability (Section 2.3). We then detail the reconstruction of three whistler wave packets from Encounter 1 (Sections 3.1–3.3). We finally discuss the applicability of the method to other encounters (Section 4.1) and apply the technique to a whistler wave packet from Encounter 2 (Section 4.2).

2. Data and Method Descriptions

2.1. Data

The payload of PSP includes a SCM (Jannet et al., 2021) that measures the 3 Hz to 1 MHz fluctuations of up to three of the orthogonal (**u**, **v**, **w**) components of the magnetic field. The SCM has three low-frequency (LF) windings, one for each component, that cover frequencies from 3 Hz to 20 kHz, and one medium-frequency (MF) winding on the **u** component that measures from 1 kHz to 1 MHz; the LF **u** winding is the component that became unusable after March 2019. After more than 3 years of operation, the SCM has revealed a multitude of different wave phenomena in the solar wind, reviewed by Dudok de Wit et al. (2022). Among them are whistler waves occurring in the solar wind over a wide range of heliocentric distances.

Complementing the SCM aboard PSP is an EFI that measures two components of the electric field from DC to 1 MHz. The EFI uses the PSP spacecraft reference frame, (**X**, **Y**, **Z**), which is different from the (**u**, **v**, **w**) SCM reference frame (Malaspina et al., 2016). A description of these various reference frames as well as the rotation matrix for transforming from the SCM frame to the spacecraft frame is presented in Appendix B. The four electric PSP EFI antennas are located in the plane of the spacecraft heat shield, which is the (**X**, **Y**) plane of the spacecraft coordinate system with the **Z** axis directed toward the Sun. These antennas, therefore, allow the measurement of the **X** and **Y** components of the electric field.

Both the SCM and EFI are a part of the PSP FIELDS suite (Bale et al., 2016; Malaspina et al., 2016). The data products from FIELDS for Encounter 1 include continuous waveforms with sampling rate of 292.97 Hz in the vicinity of perihelia (146 and 73 Hz at larger distances from the Sun) and 3.5 s burst waveform intervals with 150 kHz sampling rate (up to a few dozen a day in the vicinity of perihelia). There are also continuous cross-spectra (every 27.96 s) that enable the polarization properties of whistler waves to be determined over the frequency range of 23–4,541 Hz in 54 logarithmically spaced frequency channels. Finally, there are Band-Pass Filtered data (BPF) that provide the amplitude of the magnetic field every 0.87 s with a lower frequency resolution.

In this study, we use the survey mode waveforms (292.97 Hz) and the burst waveforms (150 kHz) of the magnetic and electric fields from the SCM and EFI. We also use data from the PSP DC fluxgate magnetometer (MAG), that measures three components of the magnetic field in spacecraft coordinates, to estimate the background magnetic field. The background plasma density and the solar wind speed are obtained from measurements made by the SWEAP Solar Probe Cup, SPAN-C (Case et al., 2020; Kasper et al., 2016).

2.2. The Reconstruction Technique

With three components of the fluctuating magnetic field the ellipticity of the wave can be obtained by the analysis of the spectral matrices (Means, 1972; Santolík et al., 2003; Taubenschuss & Santolík, 2019). The WNA

can be determined with these matrices or by a minimum variance analysis (Paschmann & Daly, 1998; Sonnerup & Cahill, 1967; Sonnerup & Scheible, 1998). These methods give the propagation angle with an ambiguity of ±180° which is removed by calculating the radial direction of propagation (sunward or anti-sunward). The latter is determined by calculating the sign of the Z component (S_Z, of the spacecraft reference frame) of the Poynting flux.

The three components of the magnetic field and the two components of the electric field can also be used with the equation $\vec{E}\mathrm{w}(\omega,t)\cdot\vec{B}\mathrm{w}(\omega,t)=0$ to find the missing component of the electric field and thus determine the Poynting flux completely.

If one of the three components of magnetic field perturbations is not measured, direct estimation of wave polarization parameters is not possible. However, if two magnetic components and two electric field components are and geometrically independent, as in the case of the SCM and EFI, it can be possible to reconstruct the missing third component of the fluctuating magnetic field; this requires knowledge of the wave dispersion and polarization properties over the range of observed perturbation frequencies. Whistler waves, as an electromagnetic plasma mode with a well-defined right-handed polarization in the frequency range from f_{lh} to f_{ce}, are a good candidate for reconstruction.

Using the cold plasma dispersion relation for whistler waves and the low-frequency and high-density limits ($\omega/\omega_{\mathrm{ce}}\ll 1$, $\omega_{\mathrm{pe}}^2\gg\omega_{\mathrm{ce}}^2$ where ω_{pe} is the local electron plasma frequency, ω the wave frequency in the plasma frame and $\omega_{\mathrm{ce}}=2\pi f_{\mathrm{ce}}$), one can show that (see details in Appendix A1):

$$\frac{|E^{\mathrm{SC}}\mathrm{w}_{\parallel}|}{|E\mathrm{w}|}\leq\left(\frac{V_{\mathrm{SW}\perp}}{V_{\varphi}}+\left(\frac{\omega}{\omega_{\mathrm{ce}}}\right)\tan\theta\right) \tag{1}$$

where $|E^{\mathrm{SC}}\mathrm{w}_{\parallel}|$ is the modulus of the electric field component along the background magnetic field $\vec{B}_0$ in the spacecraft frame. In the following, quantities with the $^{\mathrm{SC}}$ superscript are in the spacecraft frame while quantities in the plasma frame (i.e., taking into account the Lorentz transformations (Feynman, 1964)) are noted without superscript. Subscripts are used to give the reference frames, (**X**, **Y**, **Z**) corresponding to the spacecraft, (**u**, **v**, **w**) corresponding to the SCM and (∥, ⊥) corresponding to the background magnetic field. $V_{\mathrm{SW}\perp}$ is the measured perpendicular solar wind speed and V_{φ} is the wave phase speed. We note that $|E^{\mathrm{SC}}\mathrm{w}_{\parallel}|/|E\mathrm{w}|$ is small if $\omega\ll\omega_{\mathrm{ce}}$, $\tan\theta\leq 1$ and $V_{\mathrm{SW}\perp}/V_{\varphi}\ll 1$. In this case, we can make the following approximation:

$$E^{\mathrm{SC}}\mathrm{w}_{\mathrm{X}}B_{0\mathrm{X}}+E^{\mathrm{SC}}\mathrm{w}_{\mathrm{Y}}B_{0\mathrm{Y}}+E^{\mathrm{SC}}\mathrm{w}_{\mathrm{Z}}B_{0\mathrm{Z}}=E^{\mathrm{SC}}\mathrm{w}_{\parallel}\simeq 0 \tag{2}$$

The validity of this approximation and its effect on reconstruction is discussed in detail in Section 2.3. Equation 2 enables a reconstruction of the third component ($E^{\mathrm{SCre}}\mathrm{w}_{\mathrm{Z}}$) of the electric field from the measured values $E^{\mathrm{SC}}\mathrm{w}_{\mathrm{X}}$ and $E^{\mathrm{SC}}\mathrm{w}_{\mathrm{Y}}$. We note that there is a problem when the $B_{0\mathrm{Z}}$ component is close to 0 but this represents only a minority of cases in the PSP measurements.

The reconstructed electric field $\vec{E}^{\mathrm{SCre}}\mathrm{w}$ (in the spacecraft reference frame) can then be expressed in the SCM reference frame and used to reconstruct the third component of wave magnetic field $B^{\mathrm{SCre}}\mathrm{w}_{\mathrm{u}}$. For this purpose, we use the two measured components of the SCM ($B^{\mathrm{SC}}\mathrm{w}_{\mathrm{v}}$ and $B^{\mathrm{SC}}\mathrm{w}_{\mathrm{w}}$) and the electromagnetic wave equation in which the only unknown is $B^{\mathrm{SCre}}\mathrm{w}_{\mathrm{u}}$:

$$\vec{E}^{\mathrm{SCre}}\mathrm{w}(\omega,t)\cdot\vec{B}^{\mathrm{SC}}\mathrm{w}(\omega,t)\simeq 0 \tag{3}$$

The right-hand side of Equation 3 is not explicitly zero because of the approximation made in Equation 2. (ω, t) represents the time averaged Fourier transform. Equation 3 is solved in the Fourier frequency domain to take into account the whistler dispersion relation and the dependence of the estimation error on frequency. The waveform $B^{\mathrm{SCre}}\mathrm{w}_{\mathrm{u}}$ is then obtained from the inverse Fourier transform. As explained in Appendix A1, because $V_{\mathrm{SW}}\ll c$ (where c is the speed of light) we can safely consider that $\vec{B}^{\mathrm{SC}}\mathrm{w}=\vec{B}\mathrm{w}$.

It should be noted that the form of Equations 2 and 3 shows that the method is independent of the chosen effective length of the antennas. In the following, we therefore take an effective length of 3.5 m, even though this length depends on the frequency and on the propagation direction (Karbashewski et al., 2023).

2.3. Validity of the Approximation

The main approximation of this method is therefore to consider $E^{SC}\mathrm{w}_{\parallel} = 0$. An upper value of $|E^{SC}\mathrm{w}_{\parallel}|/|E\mathrm{w}|$ is given by Equation 1. We can distinguish two sources of error.

The first source of error comes from the fact that the measured electric field is different from the electric field in the plasma frame. To obtain the electric field in the plasma frame, one needs to carry out the Lorentz transformations (Feynman, 1964), which is not directly possible with only two components of the magnetic field. This error can be expressed as $\frac{V_{SW\perp}}{V_\varphi}$ and can be significant if the solar wind velocity and background magnetic field are not aligned and if the phase velocity is low.

The second source of error comes from the parallel component of the electric field in the plasma frame, which is not zero if the WNA is not equal to zero. This error can be expressed as $\left(\frac{\omega}{\omega_{ce}}\right)\tan\theta$ and can be significant if the wave is oblique or if $\frac{\omega}{\omega_{ce}}$ is large.

The propagation of these errors gives an error on the reconstructed magnetic field, whose amplitude can be approximated as follows (see details in Appendix A2):

$$(|\boldsymbol{B}^{\mathrm{error}}\mathrm{w}_u/\boldsymbol{B}\mathrm{w}|) \lesssim \sqrt{\left(\frac{V_{SW\perp}}{V_\varphi}\sin\theta\right)^2 + \left(\left(\frac{\omega}{\omega_{ce}}\right)\tan\theta\sin\theta\right)^2}\,\frac{1}{\sin\theta_{\vec{B}_0,\vec{u}}} \tag{4}$$

We note a multiplication by $\sin\theta$ (compared to Equation 1), which can be explained by the fact that the error is on the parallel component of the electric field, which is multiplied (Equation 3) by the parallel component of the magnetic field. Finally, the term $\sin\theta_{\vec{B}_0,\vec{u}}$ comes from the fact that we can't reconstruct the parallel component of the fields correctly since we are making the assumption $E^{SC}\mathrm{w}_{\parallel} = 0$. Thus, there is a problem when $\vec{\boldsymbol{B}}_0$ and $\vec{u}$ are aligned.

In Figure 1a we represent $\frac{V_{SW\perp}}{V_\varphi}\sin\theta$ in the $\left(\theta, \frac{V_{SW\perp}}{V_\varphi}\right)$ plane. The whistler wave packets measured during PSP's first encounter using burst mode are superimposed on this panel (50 wave packets were detected). We also add the characteristics of a wave packet from continuous waveforms at 292.97 Hz (point with $\theta \simeq 60°$). This wave packet is studied in detail in Section 3.3. Whistler detection and characterization methods are described in Kretzschmar et al. (2021). We note that the vast majority of points (96%) are below the 10% error line.

In Figure 1b we represent $\frac{\omega}{\omega_{ce}}\tan\theta\sin\theta$ in the $\left(\theta, \frac{\omega}{\omega_{ce}}\right)$ plane. The measured whistler characteristics are also superimposed on this panel (see Figure 1a). Note that the vast majority (99%) of points are below the 10% error line and 92% of points are below the 0.1% line. We can note that the frequency in the plasma frame of the sunward waves is generally greater than that of the anti-sunward waves (Figure 1d). This is a good indication of validity of the generation mechanism proposed by Karbashewski et al. (2023). Note that in this study we are only interested in the clearly sunward or anti-sunward cases, and do not consider the counter-streaming cases (Karbashewski et al., 2023).

The final theoretical error (given by Equation 4) is plotted as a function of $\frac{V_{SW\perp}}{V_\varphi}$ on Figure 1c using the characteristics of the measured whistler wave packets. This error is compared with the experimental error defined as $mean(|\boldsymbol{B}^{\mathrm{re}}\mathrm{w}_u - \boldsymbol{B}\mathrm{w}_u|/\max(\boldsymbol{B}\mathrm{w}_u))$. There is a good agreement between these two curves which is a good indication that the error is well estimated by Equation 4. We note that theoretical and experimental errors tend to increase with $\frac{V_{SW\perp}}{V_\varphi}$. We also observe a significant error for cases with $0.35 < \frac{V_{SW\perp}}{V_\varphi} < 0.5$ which is due to the fact that for the majority of these cases $\vec{\boldsymbol{B}}_0$ and $\vec{u}$ were almost aligned. The decrease in error for cases verifying $\frac{V_{SW\perp}}{V_\varphi} > 0.5$ is due to the fact that their WNAs are close to 0°. In addition, when the theoretical and experimental errors are large, there is a large discrepancy between the measured and reconstructed wave vectors.

For 78% of cases, the theoretical and experimental errors are less than 0.2. For these cases, the error between the measured and reconstructed wave vectors is always less than 30° with an average value of 6°. For 100% of these cases, the reconstructed direction of propagation (sunward or anti-sunward) was found to be correct. Moreover, the averaged reconstructed ellipticity is 0.80, compared with 0.85 for the measured wave packets.

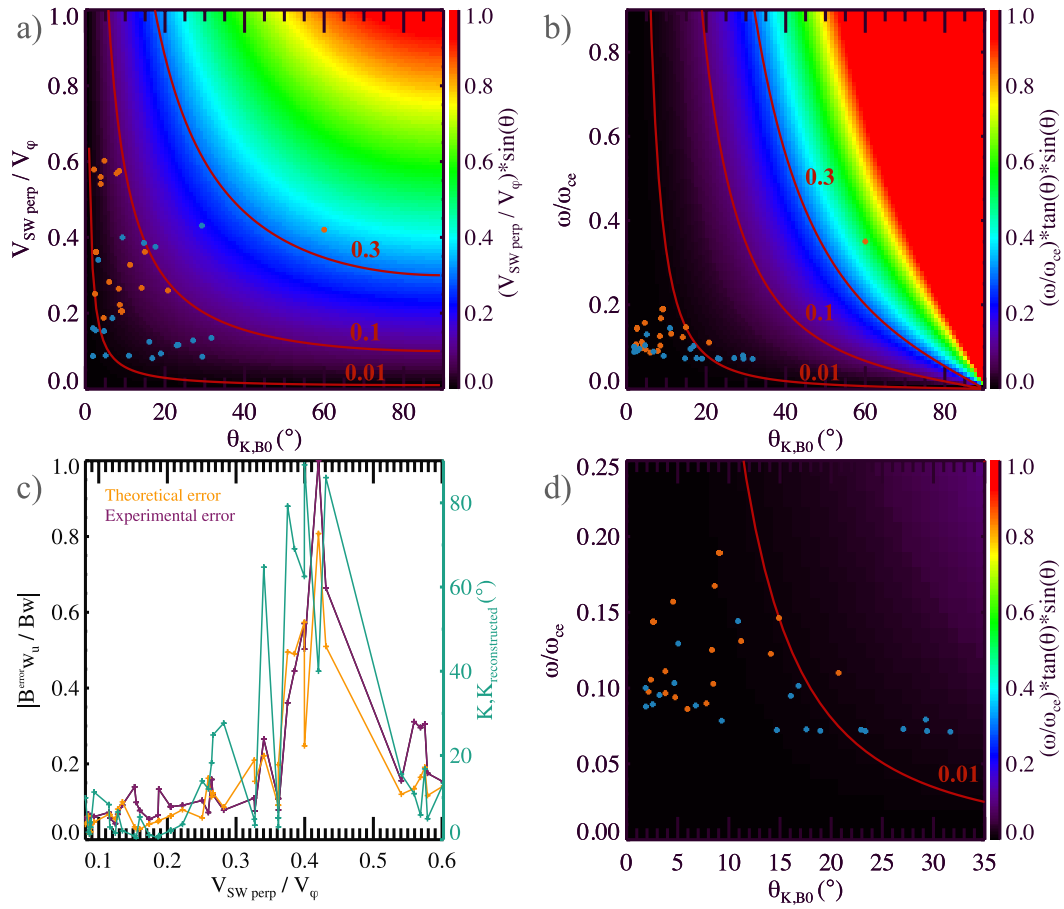

Figure 1. (a) Parameters of whistler waves in the $\left(\theta, \frac{V_{SW\perp}}{V_\varphi}\right)$ plane observed by Parker Solar Probe during encounter 1 (see text). Anti-sunward (resp., sunward) whistler waves are represented by blue (resp., orange) dots. The error due to the term $\frac{V_{SW\perp}}{V_\varphi}\sin\theta$ is indicated by the background color. (b) Parameters of whistler waves in the $(\theta, \omega/\omega_{ce})$ plane. The error due to the term $\left(\frac{\omega}{\omega_{ce}}\right)\tan\theta\sin\theta$ is indicated by the background color. (c) Theoretical and experimental errors of the reconstruction technique, as well as the angular deviation between the measured and reconstructed wave vector as a function of $\frac{V_{SW\perp}}{V_\varphi}$. (d) Zoom on the on the lower left side of the panel (b). In panels (a, c, and d) ω is the frequency in the plasma frame.

For cases where the error is greater than 0.2, large discrepancies are found between the measured and reconstructed wave vectors (up to 90°), and the sunward or anti-sunward propagation direction is found in only 65% of the cases. For these cases, the averaged reconstructed ellipticity is 0.46.

We can therefore conclude that in about 80% of the burst mode data from the first PSP encounter, the reconstruction method is applicable. When the theoretical error (given by Equation 4) is below 0.2, the technique allows to find the direction of propagation (sunward or anti-sunward) in 100% of cases and the error on the WNA is on average 6°. When the theoretical error is bigger than 0.2, the technique is not applicable and this is mainly due to a high $\frac{V_{SW\perp}}{V_\varphi}$ or a low $\theta_{\vec{B}_0,\vec{u}}$. This last source of errors can be easily checked. On the other hand, θ, V_φ and ω are no longer directly accessible after March 2019. The applicability of this method after this date is therefore discussed in detail Section 4.1.

Finally, as mentioned above, Equation 1 (and therefore Equation 4) are based on the high density hypothesis $\omega_{pe}^2 \gg \omega_{ce}^2$. Extrapolation of HELIOS data (between 0.3 and 1 AU, (Bale et al., 2016)) shows that the expected $\omega_{pe}^2/\omega_{ce}^2$ is around 150 at 10 $R_\odot$. This ratio increases with distance, indicating that this assumption should be valid for all PSP encounters.

The results of the reconstruction and its accuracy are illustrated below on three examples from Encounter 1 when all three (**u**,**v**,**w**) components of the SCM were available. Two examples demonstrate the regularly observed

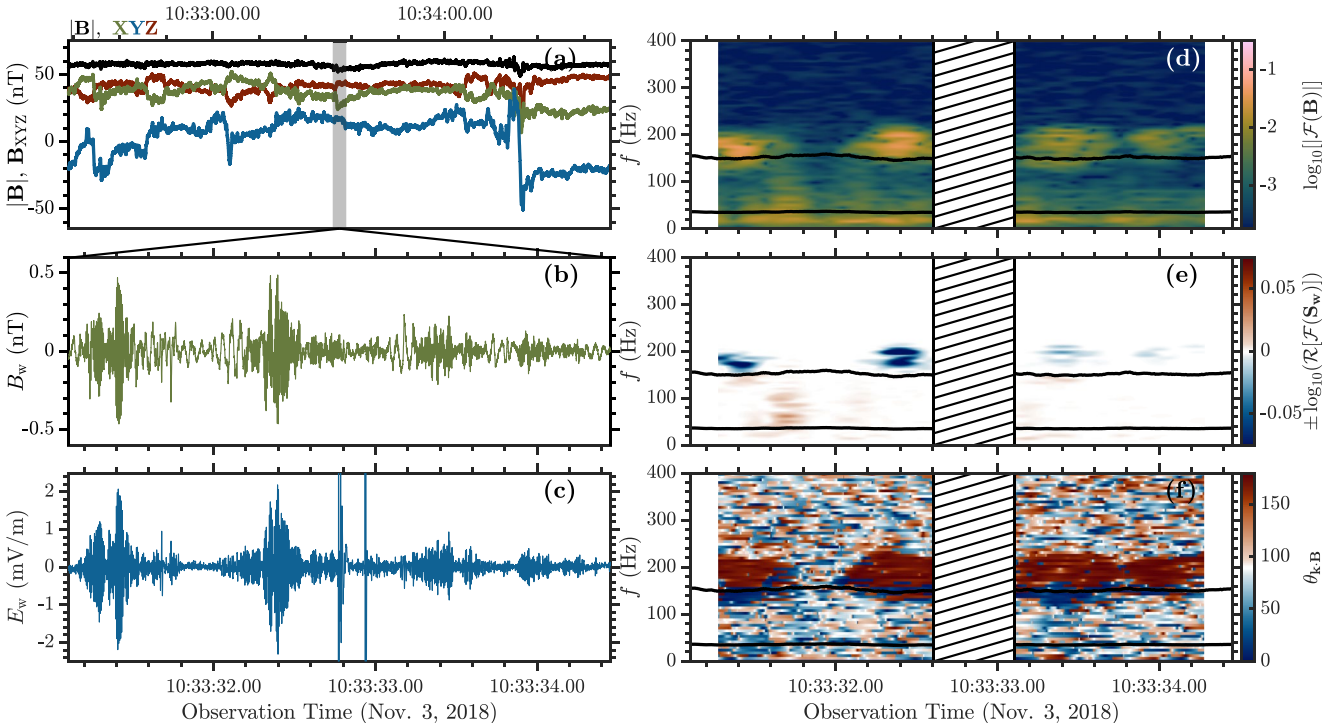

Figure 2. Whistler wave packets recorded by Parker Solar Probe on 3 November 2018. (a) Background magnetic field in the spacecraft coordinates over a short window around the burst. (b) Burst waveform of the Y magnetic field component, $B\mathrm{w}_{\mathrm{Y}}$. (c) Burst waveform of the Y electric field component, $E\mathrm{w}_{\mathrm{Y}}$. (d) Spectrogram of the magnetic field burst waveforms. (e) Z component of the Poynting flux. (f) Wave normal angle $\theta_{\mathbf{k},\mathbf{B}}$, ranging from 0° to 180° and indicating parallel (below 90°) and anti-parallel propagation (above 90°), respectively. The lower and upper solid lines in panels (d–f) indicate f_{lh} and $0.1f_{\mathrm{ce}}$, respectively. For panels (d) to (f) the frequency is shown in the spacecraft frame.

by PSP whistler wave characteristics: Case 1 and Case 2. Case 3 is atypical because of its frequency, its phase speed, and its WNA and illustrates what happens when one is out of the applicability range of the method. We provide the results of polarization analysis (the radial component of Poynting flux, WNA, ellipticity) and the power spectral density to compare with the values obtained by making use of the reconstructed $B^{\mathrm{re}}\mathrm{w}_{\mathrm{u}}$ magnetic field component. For these three examples, we first present the case using the actual measurements (Figures 2, 4, and 6) and then compare them with the results of the reconstruction (Figures 3, 5, and 7).

3. Application of the Method

3.1. Case 1: 3 November 2018, 10:33:31.0–10:33:34.5 UT

Figure 2 presents two typical anti-sunward propagating whistler wave packets, recorded at the heliocentric distance of ~41 ($\mathrm{R}_{\odot}$) in the FIELDS burst mode (150 kHz) at 10:33:31.0 UTC, 3 November 2018. This figure is adapted from Figure 9 of Karbashewski et al. (2023). The polarization parameters are directly evaluated using measurements of the three magnetic field components and the missing component of the electric field is estimated from $\vec{E}\mathrm{w}(\omega,t)\cdot\vec{B}\mathrm{w}(\omega,t)=0$ (Figures 2c and 2e). This allows us to estimate the Poynting flux vector. The Poynting flux reveals that the whistler waves are propagating from the Sun almost field-aligned, in the opposite direction to the background magnetic field (Figures 2e and 2f). These wave packets are not associated with any significant perturbation of the background magnetic field (Figure 2a), which is regular for anti-sunward propagation (Karbashewski et al., 2023). The observed wave and plasma parameters are typical of the young solar wind: the background magnetic field magnitude is 55 nT; the plasma density is ~290 cm^3; $\left(\omega_{\mathrm{pe}}/\omega_{\mathrm{ce}}\right)^2$ ~ 10,000; $\omega/\omega_{\mathrm{ce}}$ ~ 0.1 (in the plasma frame); the bulk radial plasma velocity is 310 km/s; the wave amplitudes reache 0.5 nT. The observed WNAs of the packets are below 20° (Figure 2f). The wave packets propagating anti-sunward have the wave frequency downshifted from the range 130–200 Hz (in the spacecraft frame) to 110–180 Hz (0.08–0.13 f_{ce}) in the plasma frame. The solar wind velocity perpendicular to the magnetic field $V_{\mathrm{SW}\perp}$ is about 134 km/s.

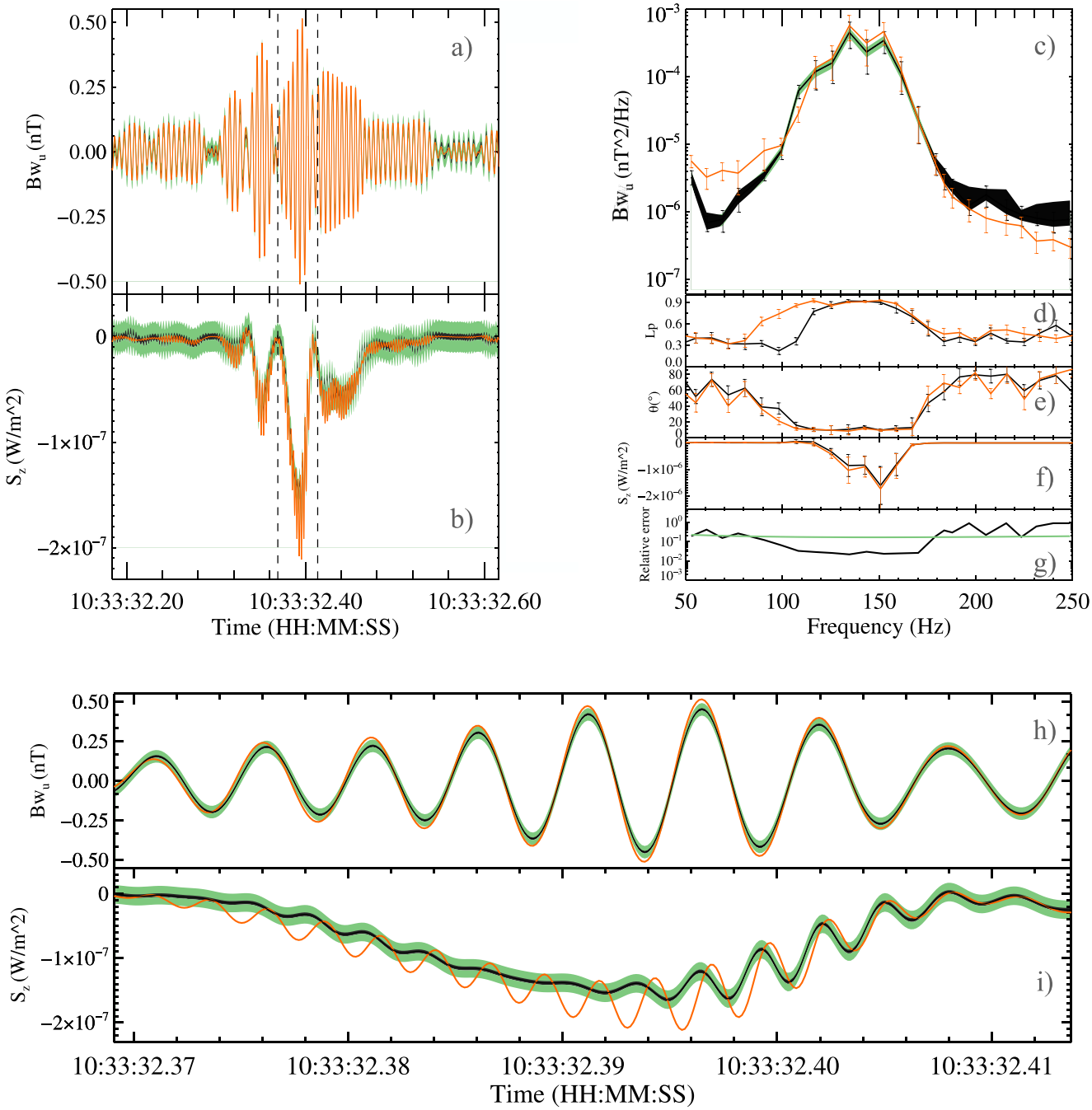

Figure 3. Comparison between the whistler wave packet recorded by Parker Solar Probe on 3 November 2018 and its reconstruction. The original data are in orange and the reconstructed ones are in black. The error bars are detailed in the text. (a) Burst waveform of the u magnetic field component. (b) Z component of the Poynting flux. The panels (c) to (g) show the frequency in the plasma frame. (c) Power spectral density of the u component. (d) Ellipticity. (e) Wave normal angle $\theta_{\mathbf{k}\cdot\mathbf{B}}$. (f) Z component of the Poynting flux. (g) - theoretical relative error in black and using a proxy of the angle of propagation in green. Panels (h and i) show a zoom on the period between the vertical dotted lines in panels (a and b).

Finally, the phase velocity is $V_\varphi \sim 893$ km/s and the component to be reconstructed for this test event satisfies the condition of being nearly perpendicular to the magnetic field $\sin\left(\theta_{\vec{u},\vec{B}_0}\right) \sim 0.99$.

The results of wave polarization reconstruction on the first wave packet are shown in Figure 3. The orange curves represent the original data, while the black and green curves are obtained using the reconstructed $B^{\mathrm{re}}w_u$ component. For Figures 3a, 3b, 3h, and 3i the thickness of the green and black lines corresponds to the estimation of

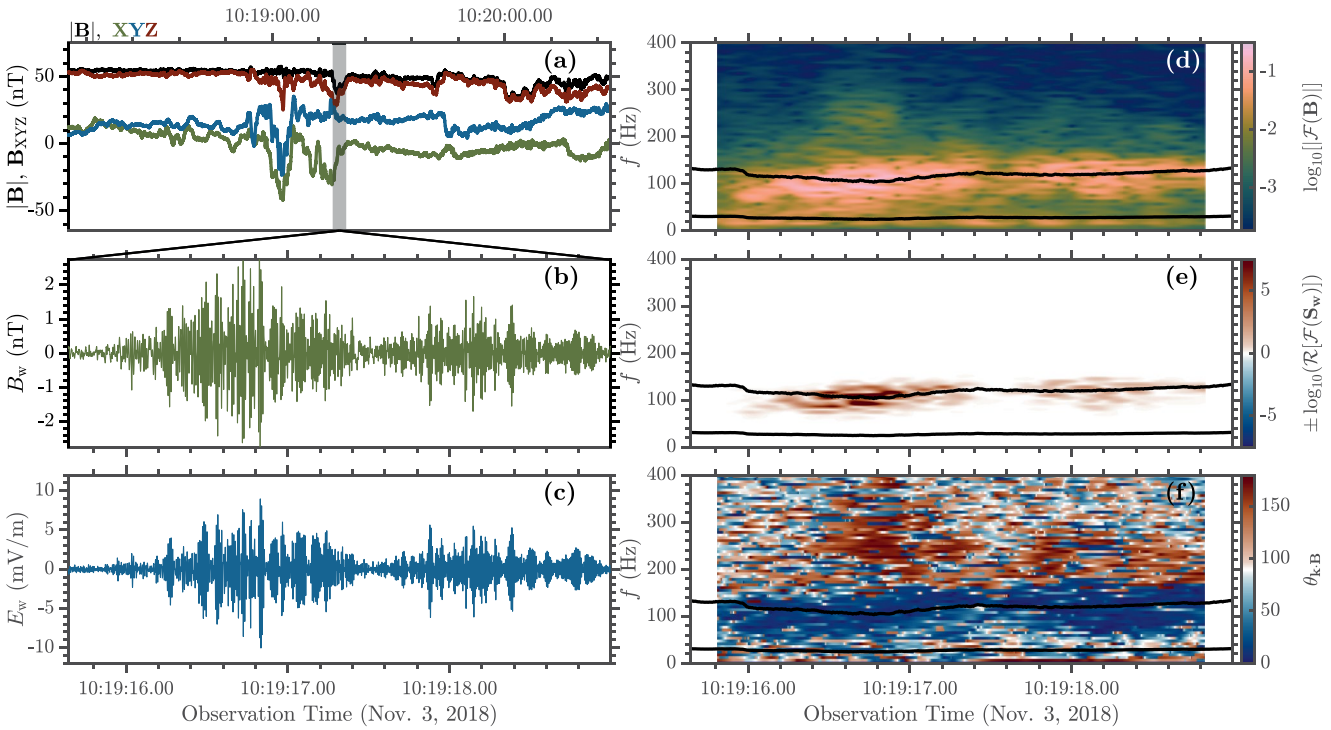

Figure 4. Whistler wave packets recorded by Parker Solar Probe on 3 November 2018. (a) Backgroud magnetic field in the spacecraft coordinates over a short window around the burst. (b) Burst waveform of the Y magnetic field component, $B\mathrm{w}_\mathrm{Y}$. (c) Burst waveform of the Y electric field component, $E\mathrm{w}_\mathrm{Y}$. (d) Spectrogram of the magnetic field burst waveform. (e) Z component of the Poynting flux. (f) Wave normal angle $\theta_{\mathbf{k}\cdot\mathbf{B}}$, ranging from 0° to 180° and indicating parallel (below 90°) and anti-parallel propagation (above 90°), respectively. The lower and upper solid lines in (d–f) indicate f_{lh} and $0.1f_{\mathrm{ce}}$, respectively. For panels (d) to (f) the frequency is shown in the spacecraft frame.

the theoretical error of the technique (Equation 4). This relative error is calculated using the typical frequency (in the plasma frame) and angle of propagation of the wave (black) and a proxy of the propagation angle in green. This proxy is estimated using the theoretical ratio $E_{\mathrm{w}\parallel}/E_{\mathrm{w}}$ in the plasma frame (Equation A9). For a given value of $\omega/\omega_{\mathrm{ce}}$ the curve $E_{\mathrm{w}\parallel}/E_{\mathrm{w}}$ as a function of θ has a plateau shape. The proxy of the WNA represents the mean value of θ on this plateau. For Figure 3c the theoretical errors (associated with each frequency and angle of propagation) are in black and using a proxy of the angle of propagation in green. These theoretical relative errors are shown in Figure 3g and are limited to 1. Figure 3c–3f the error bars correspond to the statistical errors of the computation of spectral matrices. The case satisfies very well the applicability parameters for the reconstruction: $|B^{\mathrm{error}}\mathrm{w}_\mathrm{u}/B\mathrm{w}|$ is in the range 0.02–0.05 for the entire frequency range of the whistler activity (Figure 3g). The results obtained from the reconstructed $B^{\mathrm{re}}\mathrm{w}_\mathrm{u}$ are in very good agreement with the results based on the measured $B\mathrm{w}_\mathrm{u}$. Indeed, we can see in Figures 3a, 3b, 3h, and 3i that there is a very good agreement (phase and amplitude) between the waveforms. The initially measured waveforms are very often contained in the error bars. This shows that the error is estimated adequately. Furthermore, we can see in Figures 3b, 3f, and 3i that the Z component of the Poynting vector is very well reconstructed, allowing the propagation direction to be recovered without ambiguity. We can also reconstruct the spectrum (Figure 3c) in a satisfactory manner, the whistler spectral bump is clearly identified. The measured and reconstructed ellipticity values are greater than 0.6 over the entire frequency range of the wave. The WNA θ (Figure 3f) is also in very good agreement with the measurement and the typical error on the frequency range of the wave is of the order of a degree. Finally, the minimum variance analysis gives less than 2° deviation between the wave vectors using the measured and reconstructed $B\mathrm{w}_\mathrm{u}$ (not shown).

Thus, for this anti-sunward propagating wave packet, which clearly satisfies the applicability parameters for reconstruction, the technique works effectively. Specifically, all important reconstructed parameters are in good agreement with the measurements: amplitude, ellipticity, direction of propagation, and WNA (with an error of less than 2°).

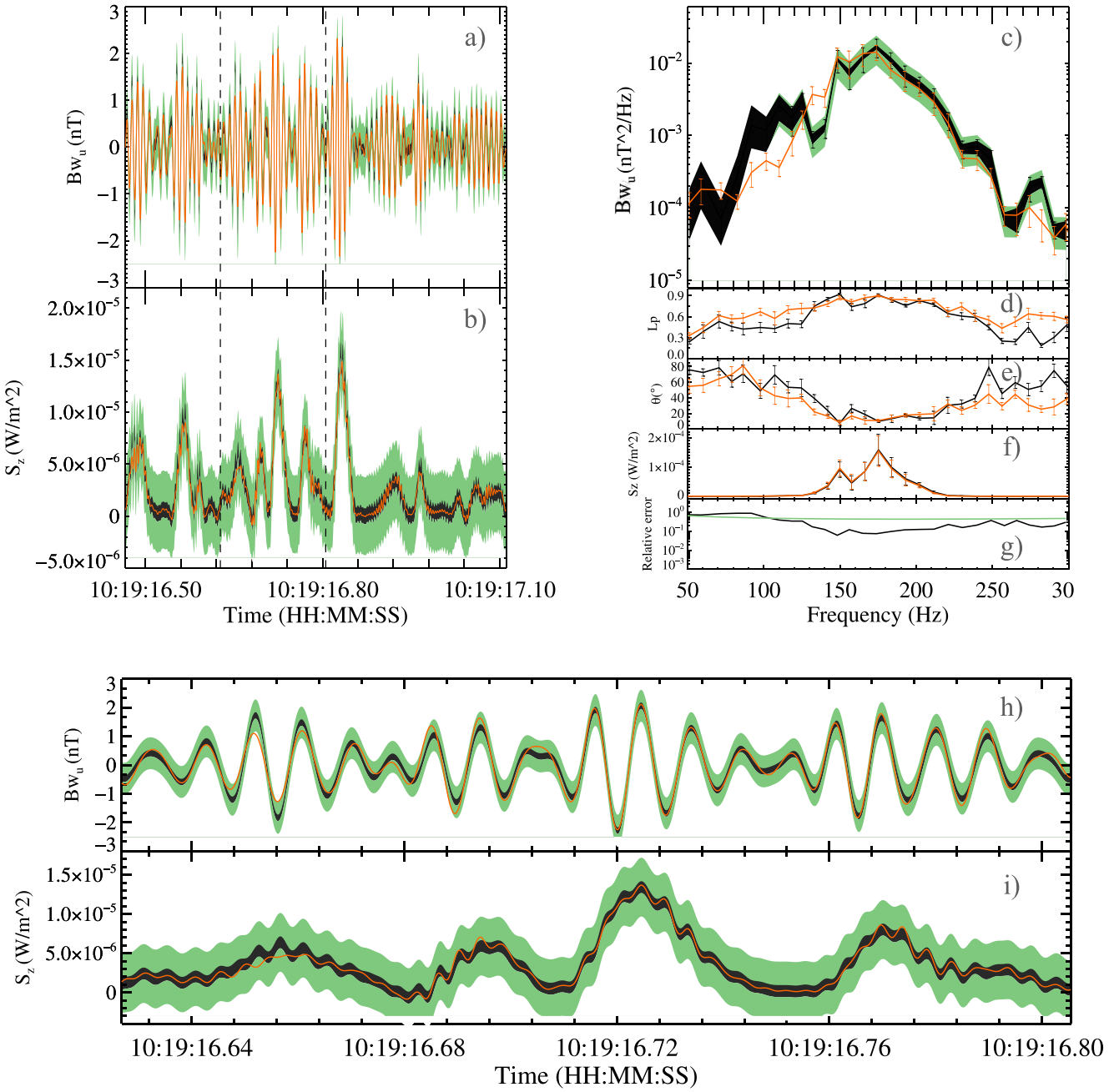

Figure 5. Comparison between the whistler wave packet recorded by Parker Solar Probe on 3 November 2018 and its reconstruction. The original data are in orange and the reconstructed ones are in black. The error bars are detailed in Section 3.1. (a) Burst waveform of the u magnetic field component. (b) Z component of the Poynting flux. The panels (c) to (g) show the frequency in the plasma frame. (c) Power spectral density of the u component. (d) Ellipticity. (e) Wave normal angle $\theta_{\mathbf{k}\cdot\mathbf{B}}$. (f) Z component of the Poynting flux. (g) Theoretical relative error in black and using a proxy of the angle of propagation in green. Panels (h and i) show a zoom on the period between the vertical dotted lines in panels (a and b).

3.2. Case 2: 3 November 2018, 10:19:15.6–10:19:19.4 UT

Figure 4 presents two typical sunward whistler wave packets, recorded at the heliocentric distance of ~41 ($R_\odot$) in the FIELDS burst mode (150 kHz) at 10:19:15.57 UTC, 3 November 2018. This figure is adapted from Figure 6 of Karbashewski et al. (2023). The polarization parameters and the missing component of the electric field are evaluated as in Section 3.1. The Poynting flux shows a sunward propagation, quasi-aligned with the background magnetic field (Figures 4e and 4f). As we can see in Figure 4a, the wave packets are associated with a dip of

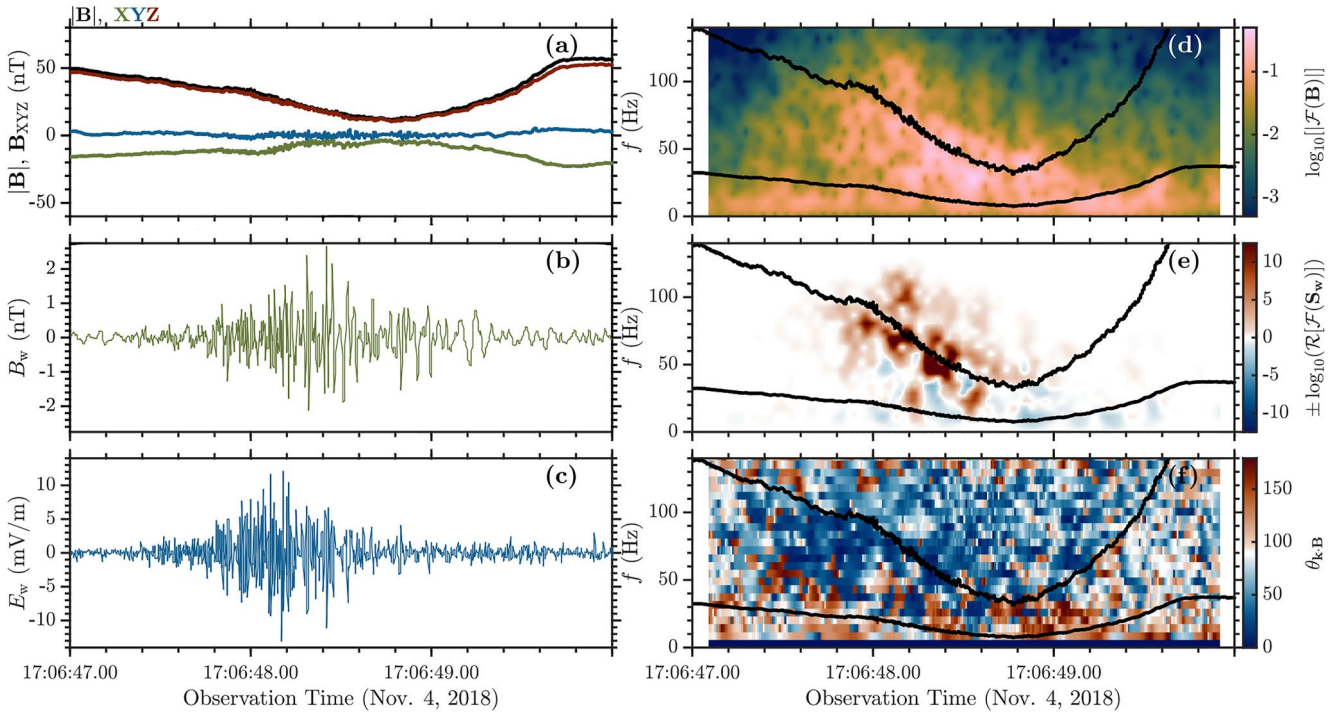

Figure 6. Whistler wave packet recorded by Parker Solar Probe on 4 November 2018. (a) Background magnetic field in spacecraft coordinates. (b) Burst waveform of the Y magnetic field component, $B\mathrm{w}_{\mathrm{Y}}$. (c) Burst waveform of the Y electric field component, $E\mathrm{w}_{\mathrm{Y}}$. (d) Spectrogram of the magnetic field burst waveform. (e) Z component of the Poynting flux. (f) Wave normal angle $\theta_{\mathbf{k}\cdot\mathbf{B}}$, ranging from 0° to 180° and indicating parallel (below 90°) and anti-parallel propagation (above 90°), respectively. The lower and upper solid lines in (d–f) indicate f_{lh} and $0.1f_{\mathrm{ce}}$, respectively. For panels (d) to (f) the frequency is shown in the spacecraft frame.

the background magnetic field of the order of 20%. This is expected for sunward whistler waves (Karbashewski et al., 2023). The background magnetic field magnitude is 48 nT; the plasma density is ~410 cm^3; $\left(\omega_{\mathrm{pe}}/\omega_{\mathrm{ce}}\right)^2 \sim$ 28,900; $\omega/\omega_{\mathrm{ce}} \sim 0.17$ (in the plasma frame); the bulk radial plasma velocity is 310 km/s; the wave amplitudes reache 2.5 nT. The observed WNAs are below 30° (Figure 4f). The wave packets propagating sunward have the wave frequency shifted from the range 60–160 Hz (in the spacecraft frame) to 120–240 Hz (0.11–0.22 f_{ce}, in the plasma frame). The solar wind velocity perpendicular to the magnetic field $V_{\mathrm{SW}\perp}$ is about 194 km/s. The phase velocity is $V_\varphi \sim$ 562 km/s and $\sin\left(\theta_{\vec{u},\vec{B}_0}\right) \sim 0.76$.

The results of wave polarization reconstruction of the first whistler wave packet are shown in Figure 5. The color code is the same as in Figure 3. This case satisfies the applicability parameters for the reconstruction: $|B^{\mathrm{error}}\mathrm{w}_{\mathrm{u}}/B\mathrm{w}|$ is in the range 0.06–0.2 for the entire frequency range of the whistler activity (Figure 5g). Because of a larger $\omega/\omega_{\mathrm{ce}}$ and a lower V_φ (which is typical for sunward whistlers, see Figure 1) the typical relative errors are about 2 times larger than for Case 1. Once again the results obtained from the reconstructed $B^{\mathrm{re}}\mathrm{w}_{\mathrm{u}}$ are in very good agreement with the results based on the measured $B\mathrm{w}_{\mathrm{u}}$ and are very similar to those described for Case 1. The reconstructed waveforms are in good agreement with those originally measured (Figures 5a, 5b, 5h and 5i). With the reconstructed data we can find without ambiguity the characteristics of a whistler wave packet propagating anti-sunward (Figures 5b, 5d, 5f, and 5i). Figure 5f shows that the error on the propagation angle is of the order of a few degrees over the frequency range of the wave. The minimum variance analysis gives less than 2° deviation between the wave vectors using the measured and reconstructed $B\mathrm{w}_{\mathrm{u}}$ (not shown).

Thus, for this sunward propagating wave packet, in the applicability range of the technique, the reconstruction works effectively. Again, all important reconstructed parameters are in good agreement with the measurements: amplitude, ellipticity, direction of propagation, and WNA (with an error of less than 2°).

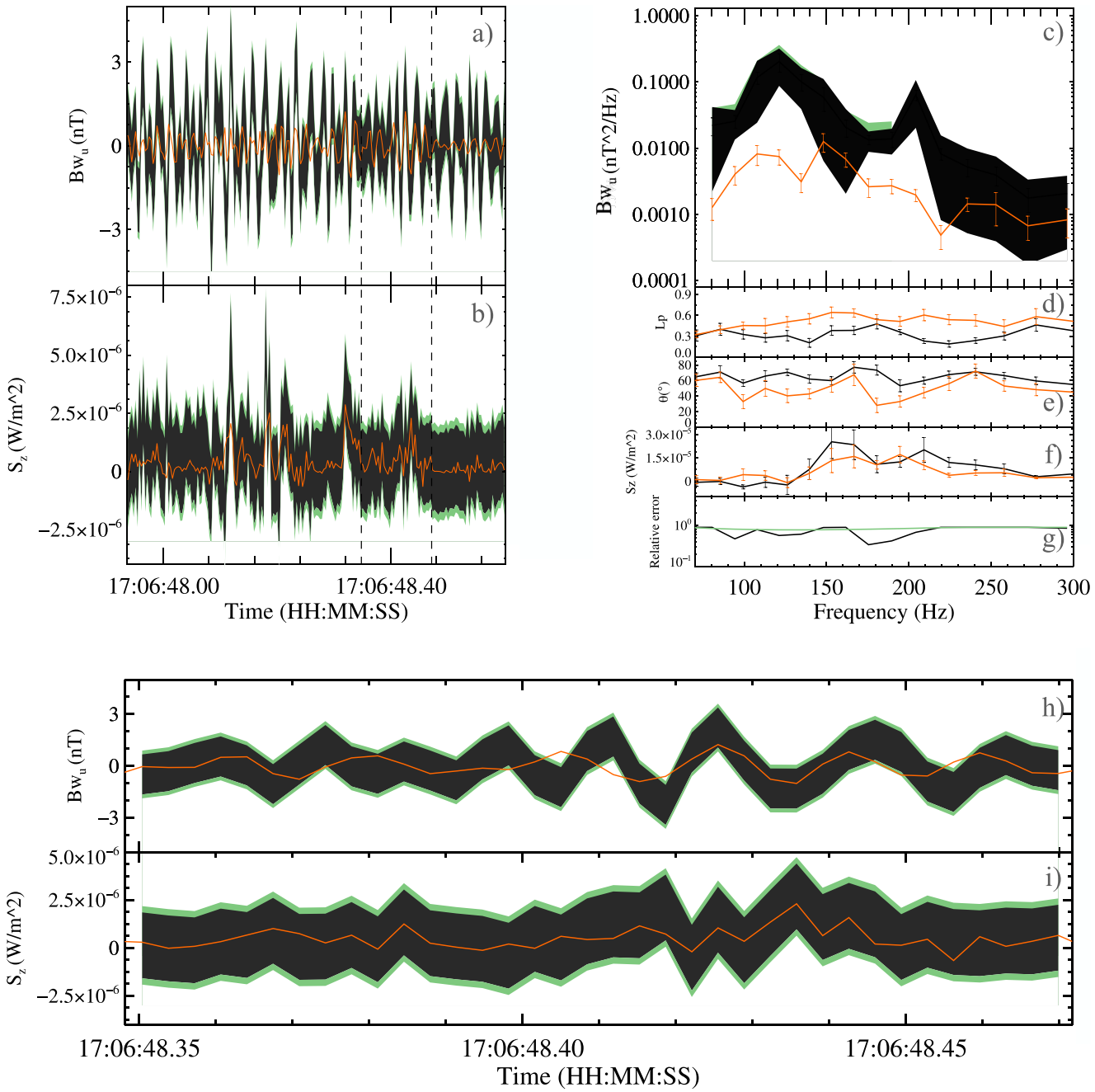

Figure 7. Comparison between the whistler wave packet recorded by Parker Solar Probe on 4 November 2018 and its reconstruction. The original data are in orange and the reconstructed ones are in black. The error bars are detailed in Section 3.1. (a) Burst waveform of the *u* magnetic field component. (b) Z component of the Poynting flux. The panels (c) to (g) show the frequency in the plasma frame. (c) Power spectral density of the *u* component. (d) Ellipticity. (e) Wave normal angle $\theta_{\mathbf{k}\cdot\mathbf{B}}$. (f) Z component of the Poynting flux. (g) Theoretical relative error in black and using a proxy of the angle of propagation in green. Panels (h and i) show a zoom on the period between the vertical dotted lines in panels (a and b).

3.3. Case 3: 4 November 2018, 17:06:47–17:06:51 UT

In Figure 6 we show the case presented in detail by Agapitov et al. (2020), recorded in waveforms with a 292.97 Hz sampling rate at 17:06:48 UTC, 4 November 2018. We can see a sunward propagating whistler with several oblique WNA sub-packets (Figures 6e and 6f). The packet is co-located with a local minimum of the background magnetic field magnitude located at a switchback boundary. The minimum $|B_0|$ value is ∼15 nT with the ambient magnetic field magnitude of ∼70 nT (Figure 6a). The corresponding enhancement of $\left(\omega_{pe}/\omega_{ce}\right)^2$ (up to 250,000

with the background value of ~10,000) inside the magnetic dip causes an unusually large Doppler shift. The wave frequency in the plasma frame is between 0.2 and 0.45 of the local f_{ce}. The solar wind velocity perpendicular to the magnetic field $V_{SW\perp}$ is about 160 km/s. The phase velocity is $V_\varphi \sim 439$ km/s and $\sin\left(\theta_{\vec{u},\vec{B}_0}\right) \sim 0.56$.

The results of wave polarization reconstruction are shown in Figure 7. The color code is the same as in Figures 3 and 5 (explained in Section 3.1). This is a difficult case for reconstruction. Indeed, as explained above the wave contains several oblique sub-packets (up to 80°, Figure 6f), and the main angle of propagation can be as oblique as 70° (Figure 7e). Moreover, we have spectral energy content up to 120 Hz (in the spacecraft frame), therefore close to the Nyquist frequency (Figures 6d and 6e). Finally, the main issues are that the wave frequency in the plasma frame is about 0.35 f_{ce} and can be up to 0.45 f_{ce}, $\frac{V_{SW\perp}}{V_\varphi}$ is about 0.35 and that $\sin\left(\theta_{\vec{u},\vec{B}_0}\right) \sim 0.56$. Therefore, taking into account the obliquity of the wave, the theoretical relative error is important: $|B^{error}w_u/Bw|$ is about 0.5 and can be greater than 1 (Figure 7g). The results obtained from the reconstructed $B^{re}w_u$ are not in good agreement with the results based on the measured Bw_u. As we can see on Figures 7a, 7b, 7h, and 7i the reconstructed waveforms do not approach the initial waveforms well. Important overestimation of the amplitude (about 3 times) is noted in the reconstructed $B^{re}w_u$ component. The Poynting flux is not perfectly recovered but the sunward direction of propagation is still clear (Figures 7b, 7f, and 7i). The reconstructed spectrum is about an order of magnitude larger than the measured one (Figure 7c). The reconstructed ellipticity is lower than 0.6 on all frequencies of the waves, which does not allow us to find the classical characteristics of a whistler wave. The propagation angle is wrong by 40° for some frequencies, which can lead to a misinterpretation of the effect of the wave on the electrons.

Thus, for this case out of the applicability range of the technique, the reconstruction doesn't work effectively. Specifically, there is an important overestimation (one order of magnitude) of the amplitude and large errors (tens of degrees) on the WNA. The ellipticity is also not well reconstructed. However, the sunward direction of propagation is clearly found.

These three cases (Case 1, Case 2, Case 3) represent a range of whistler wave parameters that can be observed by PSP during Encounter 1. Two of them (Cases 1 and 2) are within the method applicability limits. In both cases, all important reconstructed parameters are in good agreement with the measurements. Moreover, the theoretical error based on the wave frequency and using a proxy of the propagation angle is lower than the experimental error. Case 3 is an atypical case because of its high values of $f/f_{ce} \sim 0.2$–0.45, its low phase speed and, its obliquity and is out of the applicability range. In this last case, the reconstructed waveform amplitudes and the power spectral density are largely overestimated and the reconstructed WNA differs by several tens of degrees from the actual value. However, the sunward propagation direction was clearly identified.

4. Application of the Method to the Data Collected After March 2019

4.1. Discussion on the Applicability of the Method

For Encounter 2 and the following ones, we do not know the typical characteristics of the waves in the plasma frame. It is therefore not certain that the method is applicable in 80% of cases as in the first encounter. On the other hand, here are some arguments that suggest that the method should work in many cases:

First, one of the most important sources of error in the first encounters is the ratio $V_{SW\perp}/V_\varphi$. Phase velocity increases when getting closer to the Sun and should be multiplied by about 3 at 10 $R_\odot$ compared to Encounter 1 (Bale et al., 2016), which will greatly reduce the error.

Moreover, a simple Parker spiral model predicts that the background magnetic field is more radial as we get closer to the Sun. Therefore, the perpendicular component of the solar wind speed will tend to decrease. The fact that the background magnetic field is more radial should also reduce the number of configurations in which the background magnetic field is aligned with $\vec{u}$.

Another important source of error is the $(\omega/\omega_{ce})\tan\theta$ term, whose evolution cannot be predicted for the next encounters. However, Encounters 2 and 3 have similar perihelion distances and the following ones will slowly approach 10 $R_\odot$. This suggests that for at least some perihelia the waves should have similar characteristics to those observed in the first encounter. Then, as mentioned in Section 2, Cattell et al. (2022) statistics from 9 encounters showed that whistler waves frequency in the spacecraft frame was below 0.2 f_{ce} with the tendency to

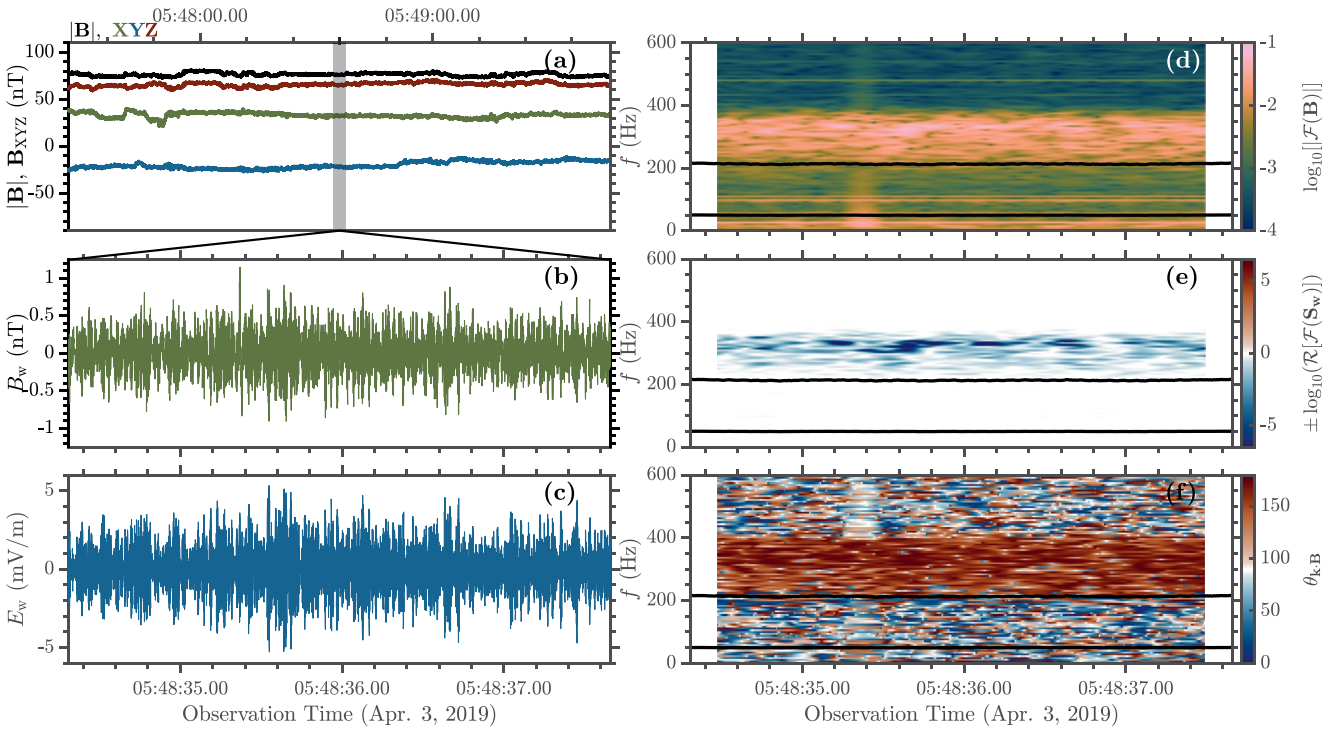

Figure 8. Whistler wave packet recorded by Parker Solar Probe on 3 April 2019. (a) Background magnetic field in spacecraft coordinates over a short window around the burst. (b) Burst waveform of the Y magnetic field component, $B\mathrm{w}_\mathrm{Y}$. (c) Burst waveform of the Y electric field component, $E\mathrm{w}_\mathrm{Y}$. (d) Spectrogram of the magnetic field burst waveform. (e) Z component of the Poynting flux. (f) Reconstructed wave normal angle $\theta_{\mathbf{k}\cdot\mathbf{B}}$, ranging from 0° to 180° and indicating parallel (below 90°) and anti-parallel propagation (above 90°), respectively. The lower and upper solid lines in (d–f) indicate f_{lh} and $0.1f_{\mathrm{ce}}$, respectively. For panels (d) to (f) the frequency is shown in the spacecraft frame.

decrease below 0.1 approaching the Sun. Figure 1b shows that in the case where $\omega/\omega_{\mathrm{ce}} \leq 0.1$ this term gives an error of less than 30% with WNAs up to 70°.

In addition, there are several pre- and post-reconstruction methods that give indications of the quality of the reconstruction. These methods are not definitive proofs but can be used as good indicators of correct reconstruction.

One can use a pre-check based on $\omega/\omega_{\mathrm{ce}}$ in the spacecraft frame (as the phase velocity increases, the measured $\omega/\omega_{\mathrm{ce}}$ becomes closer to the one in the plasma frame). By using a proxy for the propagation angle (based on $\omega/\omega_{\mathrm{ce}}$) and the ratio $\omega_{\mathrm{pe}}/\omega_{\mathrm{ce}}$ it is possible to calculate the phase velocity and derive the theoretical error using Equation 4.

Moreover, outside the range of applicability, we do not expect to reconstruct a good circular polarization (see Section 2.3). The circular polarization can therefore be used as a post-reconstruction indicator of the method's effectiveness.

4.2. Application of the Reconstruction Technique to Whistler Waves Recorded During Encounter 2 (no $B\mathrm{w}_\mathrm{u}$ Measurements): 2019/04/03, 05:48:35–05:48:37 UT

Figures 8 and 9 present a reconstructed whistler wave packet from Encounter 2, recorded at the heliocentric distance of ~37 ($\mathrm{R}_\odot$) in the FIELDS burst mode (150 kHz) at 05:48:35 UTC, 4 April 2019. The background magnetic field magnitude is 73 nT; the plasma density is ~170 cm^3; $\left(\omega_{\mathrm{pe}}/\omega_{\mathrm{ce}}\right)^2 \sim 3250$; the bulk radial plasma velocity is 310 km/s; and $\sin\left(\theta_{\vec{u},\vec{B}_0}\right) = 0.98$. The WNA, direction of propagation, and frequency in the plasma reference frame are unknown without reconstruction due to the technical issue on the u component since March 2019. Figures 8e, 9b, 9b, and 9i show that the reconstructed propagation direction is anti-sunward. The reconstructed WNA is less than 30° (Figures 8f and 9e) and the reconstructed planarity is bigger than 0.6 over the whole frequency range of the wave (Figure 9d). We can therefore deduce that $\frac{V_{\mathrm{SW}\perp}}{V_\varphi^{\mathrm{re}}} \sim 0.06$ and $f/f_{\mathrm{ce}} \sim 0.13$ (in the plasma frame). The reconstructed components thus show that we are well within the range of application of

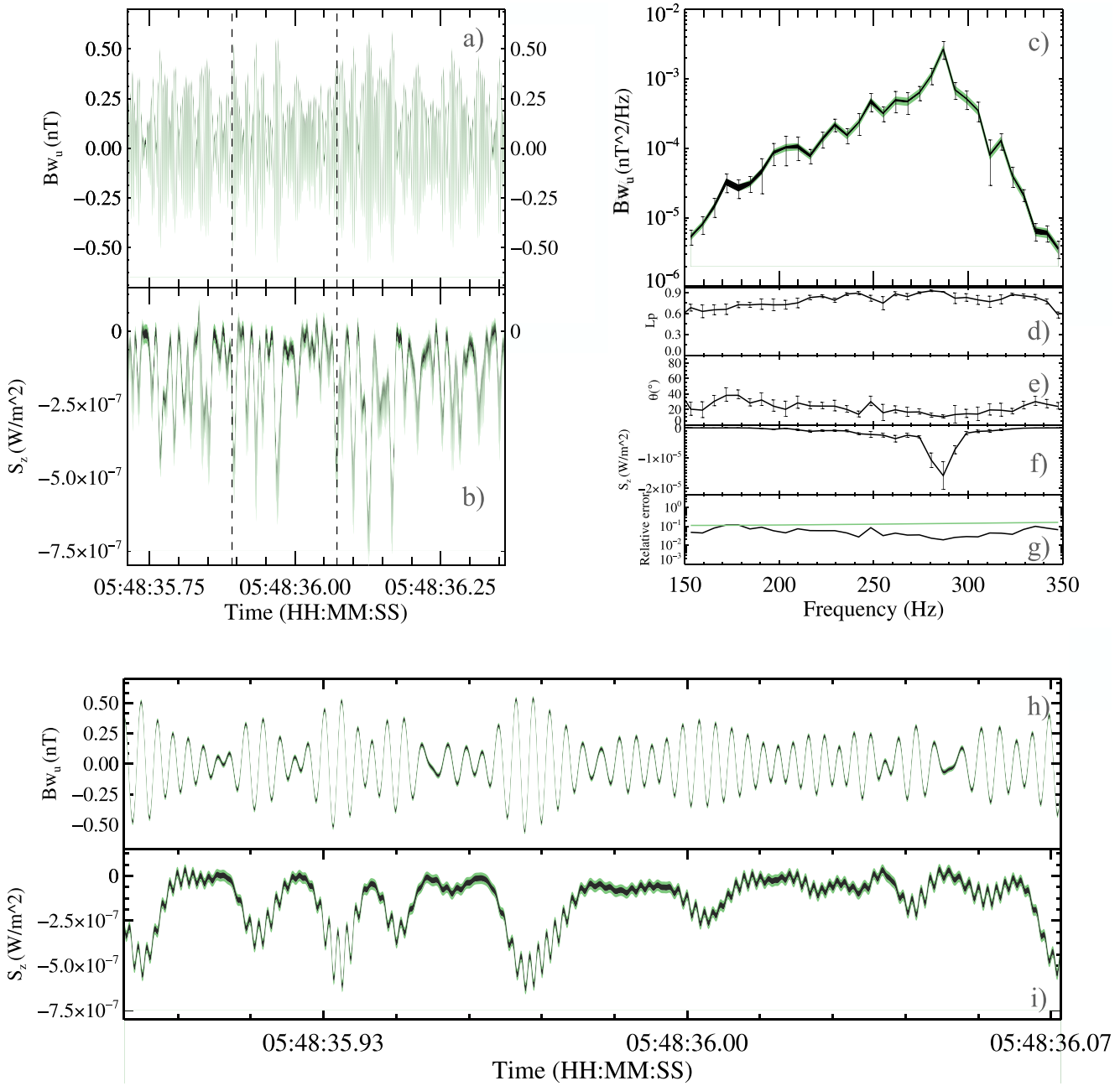

Figure 9. Reconstructed whistler wave packet recorded by Parker Solar Probe on 3 April 2019. The error bars are detailed in Section 3.1. (a) Burst waveform of the u magnetic field component. (b) Z component of the Poynting flux. The panels (c) to (g) show the frequency in the plasma frame. (c) Power spectral density of the u component. (d) Ellipticity. (e) Wave normal angle $\theta_{\mathbf{k}\cdot\mathbf{B}}$. (f) Z component of the Poynting flux. (g) Theoretical relative error in black and using a proxy of the angle of propagation in green. Panels (h and i) show a zoom on the period between the vertical dotted lines in panels (a and b).

the method and $|B^{\text{error}}w_u/Bw|$ is in the range of 0.03–0.1 (Figure 9g). The method proposed in Section 4.1 using a proxy for the propagation angle also shows that we're within the range of application (relative error less than 0.1). Moreover, ellipticity close to 1 is a good indication of correct reconstruction.

5. Conclusions

The PSP mission will last until 2025 and 24 perihelia are expected to be completed, approaching down to 10 $R_\odot$ and probing in situ regions where no direct measurements have ever been made. One component of the magnetic

field measured by the SCM is unavailable at low frequency after Encounter 1 because of a technical issue. We propose a method to determine whistler wave polarization despite the missing component. This makes it possible to evaluate wave-particle interaction effects for dynamics of the solar wind electron populations.

To conclude:

1. We develop a technique to reconstruct the polarization parameters of whistler waves based on only two components of magnetic and electric field measurements (the PSP fields measurement regime after March 2019). We reconstruct the missing components by neglecting the electric field parallel to the background magnetic field.
2. This technique is applicable with the assumptions of (a) low-frequency whistlers in the plasma frame relative to the electron cyclotron frequency; (b) a small propagation angle with respect to the background magnetic field; and (c) a large wave phase speed relative to the cross-field solar wind velocity. Critically, the method cannot be applied if the background magnetic field is aligned with the affected SCM coil.
3. When within the range of applicability, all polarization parameters could be found, including propagation direction, WNA, and ellipticity. We propose pre- and post-reconstruction methods to estimate the quality of the reconstruction. One of them is to check that the ellipticity of the reconstructed magnetic field is close to 1.
4. Our method will enable polarization properties of whistler waves in the young Solar to be determined. These polarization properties are necessary for a better understanding of particle-wave interactions.

Appendix A: Estimation of the Error of the Reconstruction Technique

A1. Estimation of the Parallel Electric Field Component in the Spacecraft Frame

In this section, we derive Equation 1.

Let us make calculations in the reference frame where $\vec{B}_0$ is directed along the **z** axis, and the **k**-vector is in the plane (**x**, **y**). Therefore, we have: $\mathbf{k} = k(\sin\theta\cos\varphi, \sin\theta\sin\varphi, \cos\theta)$, with φ the angle between **x** and **k**. To begin with, we shall treat the waves at frequencies much larger than the lower hybrid frequency (well verified for whistler waves in the solar wind) and using the cold plasma approximation. In our reference frame the dielectric tensor ε_{ij} reads:

$$\varepsilon_{ij} = \begin{pmatrix} \varepsilon_1 & i\varepsilon_2 & 0 \\ -i\varepsilon_2 & \varepsilon_1 & 0 \\ 0 & 0 & \varepsilon_3 \end{pmatrix} \tag{A1}$$

where using the typical conditions of observations $\omega_{pe}^2 \gg \omega_{ce}^2 > \omega^2$:

$$\varepsilon_1 = -\frac{\omega_{pe}^2}{\omega^2-\omega_{ce}^2}; \varepsilon_2 = \frac{\omega_{pe}^2\omega_{ce}}{\omega(\omega^2-\omega_{ce}^2)}; \varepsilon_3 = -\frac{\omega_{pe}^2}{\omega^2}$$

One can find for whistler waves:

$$N^2 = \frac{\omega_{pe}^2}{\omega(\omega_{ce}|\cos\theta| - \omega)}$$

$$\omega = \omega_{ce}|\cos\theta|\frac{\frac{k^2c^2}{\omega_{pe}^2}}{\left(1+\frac{k^2c^2}{\omega_{pe}^2}\right)}$$

The next step is to determine the polarization properties. In the following, we use $E\mathrm{w}(\omega, t)$ and $B\mathrm{w}(\omega, t)$ ((ω, t) representing the time averaged Fourier components) to approximate the theoretical fields of the general dispersion relation. We drop the (ω, t) to simplify the notations.

$$\begin{pmatrix} \varepsilon_1 - N_y^2 - N_z^2 & i\varepsilon_2 + N_xN_y & N_xN_z \\ -i\varepsilon_2 + N_xN_y & \varepsilon_1 - N_x^2 - N_z^2 & N_yN_z \\ N_xN_z & N_yN_z & \varepsilon_3 - N_x^2 - N_y^2 \end{pmatrix} \begin{matrix} E\mathrm{w}_x \\ E\mathrm{w}_y \\ E\mathrm{w}_z \end{matrix} = 0 \tag{A2}$$

$$\begin{pmatrix} \varepsilon_1 - N^2\left(\cos^2\theta + \sin^2\theta\sin^2\varphi\right) & i\varepsilon_2 + N^2\sin^2\theta\sin\varphi\cos\varphi & N^2\cos\theta\sin\theta\cos\varphi \\ -i\varepsilon_2 + N^2\sin^2\theta\sin\varphi\cos\varphi & \varepsilon_1 - N^2\left(\cos^2\theta + \sin^2\theta\cos^2\varphi\right) & N^2\cos\theta\sin\theta\sin\varphi \\ N^2\cos\theta\sin\theta\cos\varphi & N^2\cos\theta\sin\theta\sin\varphi & \varepsilon_3 - N^2\sin^2\theta \end{pmatrix} \begin{matrix} E\mathrm{w_x} \\ E\mathrm{w_y} \\ E\mathrm{w_z} \end{matrix} = 0 \quad \text{(A3)}$$

$$\begin{pmatrix} -\frac{\omega_{pe}^2}{\omega^2-\omega_{ce}^2} - N^2\left(\cos^2\theta + \sin^2\theta\sin^2\varphi\right) & i\frac{\omega_{pe}^2\omega_{ce}}{\omega\left(\omega^2-\omega_{ce}^2\right)} + N^2\sin^2\theta\sin\varphi\cos\varphi & N^2\cos\theta\sin\theta\cos\varphi \\ -i\frac{\omega_{pe}^2\omega_{ce}}{\omega\left(\omega^2-\omega_{ce}^2\right)} + N^2\sin^2\theta\sin\varphi\cos\varphi & -\frac{\omega_{pe}^2}{\omega^2-\omega_{ce}^2} - N^2\left(\cos^2\theta + \sin^2\theta\cos^2\varphi\right) & N^2\cos\theta\sin\theta\sin\varphi \\ N^2\cos\theta\sin\theta\cos\varphi & N^2\cos\theta\sin\theta\sin\varphi & -\frac{\omega_{pe}^2}{\omega^2} - N^2\sin^2\theta \end{pmatrix} \begin{matrix} E\mathrm{w_x} \\ E\mathrm{w_y} \\ E\mathrm{w_z} \end{matrix} = 0 \quad \text{(A4)}$$

Polarization vectors can be expressed in the reference frame determined at the beginning as:

$$\vec{E}\mathrm{w} = a\begin{pmatrix} \frac{\omega}{\left(\omega^2-\omega_{ce}^2\right)}\left(i\omega_{ce}\sin\varphi + \omega\cos\varphi\right) + \frac{k^2c^2}{\omega_{pe}^2}\cos\varphi \\ \frac{\omega}{\omega^2-\omega_{ce}^2}\left(\omega\sin\varphi - i\omega_{ce}\cos\varphi\right) + \frac{k^2c^2}{\omega_{pe}^2}\sin\varphi \\ \frac{\frac{k^2c^2}{\omega_{pe}^2}\cos\theta\sin\theta}{\left(1+\frac{k^2c^2}{\omega_{pe}^2}\sin^2\theta\right)}\left(\frac{\omega^2}{\left(\omega^2-\omega_{ce}^2\right)} + \frac{k^2c^2}{\omega_{pe}^2}\right) \end{pmatrix} \quad \text{(A5)}$$

$$\vec{B}\mathrm{w} = a\frac{k}{\omega}\begin{pmatrix} -\frac{\cos\theta\sin\varphi}{\left(1+\frac{k^2c^2}{\omega_{pe}^2}\sin^2\theta\right)}\left(\frac{\omega^2}{\left(\omega^2-\omega_{ce}^2\right)} + \frac{k^2c^2}{\omega_{pe}^2}\right) + i\frac{\omega_{ce}\omega\cos\theta\cos\varphi}{\omega^2-\omega_{ce}^2} \\ \frac{i\omega_{ce}\omega\cos\theta\sin\varphi}{\left(\omega^2-\omega_e^2\right)} + \left(\frac{\omega^2}{\left(\omega^2-\omega_{ce}^2\right)} + \frac{k^2c^2}{\omega_{pe}^2}\right)\frac{\cos\theta\cos\varphi}{\left(1+\frac{k^2c^2}{\omega_{pe}^2}\sin^2\theta\right)} \\ -i\frac{\omega_{ce}\omega\sin\theta}{\omega^2-\omega_{ce}^2} \end{pmatrix} \quad \text{(A6)}$$

where a is a constant. Using the refractive index magnitude, one can re-write wave polarization dependence upon characteristic frequencies as follows:

$$\vec{E}\mathrm{w} = a\begin{pmatrix} \frac{\omega}{\left(\omega^2-\omega_{ce}^2\right)}\left(i\omega_{ce}\sin\varphi + \omega\cos\varphi\right) + \frac{\omega}{\omega_{ce}\cos\theta-\omega}\cos\varphi \\ \frac{\omega}{\omega^2-\omega_{ce}^2}\left(\omega\sin\varphi - i\omega_{ce}\cos\varphi\right) + \frac{\omega}{\omega_{ce}\cos\theta-\omega}\sin\varphi \\ \frac{\omega\sin\theta}{\left(\omega_{ce}-\omega\cos\theta\right)}\left(\frac{\omega^2}{\left(\omega^2-\omega_{ce}^2\right)} + \frac{\omega}{\omega_{ce}\cos\theta-\omega}\right) \end{pmatrix} \quad \text{(A7)}$$

$$\vec{B}\mathrm{w} = a\frac{k}{\omega}\begin{pmatrix} -\frac{\left(\omega_{ce}\cos\theta-\omega\right)\sin\varphi}{\left(\omega_{ce}-\omega\cos\theta\right)}\left(\frac{\omega^2}{\left(\omega^2-\omega_{ce}^2\right)} + \frac{\omega}{\omega_{ce}\cos\theta-\omega}\right) + i\frac{\omega_{ce}\omega\cos\theta\cos\varphi}{\omega^2-\omega_{ce}^2} \\ \frac{i\omega_{ce}\omega\cos\theta\sin\varphi}{\left(\omega^2-\omega_e^2\right)} + \left(\frac{\omega^2}{\left(\omega^2-\omega_{ce}^2\right)} + \frac{\omega}{\omega_{ce}\cos\theta-\omega}\right)\frac{\left(\omega_{ce}\cos\theta-\omega\right)\cos\varphi}{\left(\omega_{ce}-\omega\cos\theta\right)} \\ -i\frac{\omega_{ce}\omega\sin\theta}{\omega^2-\omega_{ce}^2} \end{pmatrix} \quad \text{(A8)}$$

Now one can come to simplifications. We have already noted that the overwhelming majority of observed waves satisfy the condition $\omega \ll \omega_{ce}$, that is, the parameter $\frac{\omega}{\omega_{ce}} = \epsilon$ is small. This allows one to use it as the small parameter constructing solutions as power series over this parameter. The first order approximation on ϵ results in:

$$\vec{E}\mathrm{w} = a\begin{pmatrix} \frac{\omega}{\omega_{ce}}\left(-i\sin\varphi + \frac{\cos\varphi}{\cos\theta}\right) \\ \frac{\omega}{\omega_{ce}}\left(i\cos\varphi + \frac{\sin\varphi}{\cos\theta}\right) \\ \frac{\omega^2\sin\theta}{\omega_{ce}^2\cos\theta} \end{pmatrix} \quad \text{(A9)}$$

$$\vec{B}\mathrm{w} = a\frac{k}{\omega}\begin{pmatrix} -\frac{\omega}{\omega_{ce}}(\sin\varphi + i\cos\theta\cos\varphi) \\ \frac{\omega}{\omega_{ce}}(-i\cos\theta\sin\varphi + \cos\varphi) \\ i\frac{\omega}{\omega_{ce}}\sin\theta \end{pmatrix} \tag{A10}$$

The electric field is measured in the spacecraft frame, which is different from the plasma frame. It is therefore necessary to take Lorentz transformations into account. For the magnetic field, since the measured solar wind speed (V_{SW}) verifies $V_{SW} \ll c$ (where c is the speed of light) these transformations can be neglected and we can safely consider that $\vec{B}^{SC}\mathrm{w} = \vec{B}\mathrm{w}$. For the electric field, on the other hand, we have:

$$\vec{E}^{SC}\mathrm{w} = \vec{E}\mathrm{w} - \left(\vec{V}_{SW} \times \vec{B}\mathrm{w}\right) \tag{A11}$$

where $\vec{V}_{SW}$ is expressed as:

$$\vec{V}_{SW} = \begin{matrix} V_{SW\,x} \\ V_{SW\,y} \\ V_{SW\,z} \end{matrix} \tag{A12}$$

$$\left(\vec{V}_{SW} \times \vec{B}\mathrm{w}\right) = a\frac{k}{\omega}\begin{pmatrix} \frac{\omega}{\omega_{ce}}\left(i\sin\theta V_{SW\,y} - V_{SW\,z}(-i\cos\theta\sin\varphi + \cos\varphi)\right) \\ \frac{\omega}{\omega_{ce}}(-V_{SW\,z}(\sin\varphi + i\cos\theta\cos\varphi) - i\sin\theta V_{SW\,x}) \\ \frac{\omega}{\omega_{ce}}\left(V_{SW\,x}(-i\cos\theta\sin\varphi + \cos\varphi) + V_{SW\,y}(\sin\varphi + i\cos\theta\cos\varphi)\right) \end{pmatrix} \tag{A13}$$

Therefore,

$$\left|\left(\vec{V}_{SW} \times \vec{B}\mathrm{w}\right)_z\right| = a\frac{k}{\omega}\frac{\omega}{\omega_{ce}}\left(\left(V_{SW\,x}\cos\varphi + V_{SW\,y}\sin\varphi\right)^2 + \cos^2\theta\left(V_{SW\,y}\cos\varphi - V_{SW\,x}\sin\varphi\right)^2\right)^{1/2} \tag{A14}$$

By choosing, $\varphi = 0$, then

$$\left|\left(\vec{V}_{SW} \times \vec{B}\mathrm{w}\right)_z\right| = a\frac{k}{\omega}\frac{\omega}{\omega_{ce}}\left(V_{SW\,x}^2 + V_{SW\,y}^2\cos^2\theta\right)^{1/2} \tag{A15}$$

Thus,

$$|E^{SC}\mathrm{w}_{\parallel}| \leq |E\mathrm{w}|\left(\frac{V_{SW\perp}}{V_\varphi} + \left(\frac{\omega}{\omega_{ce}}\right)\tan\theta\right) \tag{A16}$$

A2. Propagation of the Error

The electromagnetic wave equation is expressed as:

$$\vec{E}\mathrm{w} \cdot \vec{B}\mathrm{w} = 0 \tag{A17}$$

and is also valid in the spacecraft frame:

$$\vec{E}^{SC}\mathrm{w} \cdot \vec{B}^{SC}\mathrm{w} = 0 \tag{A18}$$

Therefore,

$$\vec{E}^{SC}\mathrm{w}\| \cdot \vec{B}^{SC}\mathrm{w}\| + \vec{E}^{SC}\mathrm{w}\perp \cdot \vec{B}^{SC}\mathrm{w}\perp = 0 \tag{A19}$$

In our approximation we neglect $\vec{E}^{SC}\mathrm{w}\|$, therefore using results from the previous section we find

$$|\vec{E}^{SC\,re}\mathrm{w} \cdot \vec{B}^{SC}\mathrm{w}| \leq |E\mathrm{w}|\left(\frac{V_{SW\perp}}{V_\varphi} + \left(\frac{\omega}{\omega_{ce}}\right)\tan\theta\right)\sin\theta \tag{A20}$$

One way of approximating the error on the reconstructed component, considering these two errors as independent and following a normal distribution, is as follows:

$$(|B^{\text{error}}\text{w}_\text{u}/B\text{w}|) \lesssim \sqrt{\left(\frac{V_{\text{SW}\perp}}{V_\varphi}\right)^2 + \left(\left(\frac{\omega}{\omega_{\text{ce}}}\right)\tan\theta\right)^2}\,\frac{\sin\theta}{\sin\theta_{\vec{B}_0,\vec{u}}} \tag{A21}$$

Appendix B: Coordinate Transforms Between the Search-Coil Magnetometer and the Spacecraft Reference Frames

Figure B1 represents the relationship between the SCM and the spacecraft reference frame. The rotation matrix between these two frames is the following:

$$R_{\text{SCM}\to\text{SC}_{\text{ij}}} = \begin{pmatrix} 0.81654 & -0.40827 & -0.40827 \\ 0 & -0.70715 & 0.70715 \\ -0.57729 & -0.57729 & -0.57729 \end{pmatrix} \tag{B1}$$

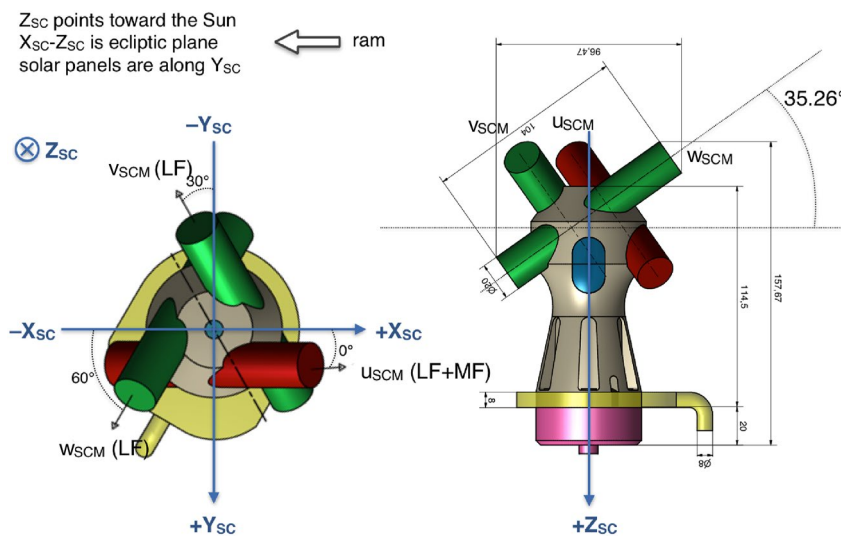

Figure B1. Schematics of the search-coil magnetometer and of the relation between its reference frame (**u**,**v**,**w**) and the one of the spacecraft (**X**,**Y**,**Z**).

Data Availability Statement

The data used in this work are available on the public data archive NASA CDAWeb (https://cdaweb.gsfc.nasa.gov/index.html/).

Acknowledgments
V.K., T.D., L.C., and M.K. acknowledge funding from the CNES. L.C., V.K., and O.V.A. were supported by NASA Grants 80NSSC20K0697 and 80NSSC21K1770. O.V.A and S.K. were partially supported by NSF Grant 1914670, NASA's Living with a Star (LWS) program (contract 80NSSC20K0218), and NASA grants contracts 80NNSC19K0848, 80NSSC22K0433, 80NSSC22K0522. Parker Solar Probe was designed, built, and is now operated by the Johns Hopkins Applied Physics Laboratory as part of NASA's Living with a Star (LWS) program (contract NNN06AA01C). We thank the FIELDS team for providing data (PI: Stuart D. Bale, UC Berkeley).

References

Agapitov, O. V., Drake, J. F., Swisdak, M., Bale, S. D., Horbury, T. S., Kasper, J. C., et al. (2022). Flux rope merging and the structure of switchbacks in the solar wind. *The Astrophysical Journal*, *925*(2), 213. https://doi.org/10.3847/1538-4357/ac4016

Agapitov, O. V., Dudok de Wit, T., Mozer, F. S., Bonnell, J. W., Drake, J. F., Malaspina, D., et al. (2020). Sunward-propagating Whistler waves collocated with localized magnetic field holes in the solar wind: *Parker Solar Probe* observations at 35.7 *R* radii. *The Astrophysical Journal*, *891*(1), L20. https://doi.org/10.3847/2041-8213/ab799c

Artemyev, A., Agapitov, O., Mourenas, D., Krasnoselskikh, V., Shastun, V., & Mozer, F. (2016). Oblique Whistler-mode waves in the Earth's inner magnetosphere: Energy distribution, origins, and role in radiation belt dynamics. *Space Science Reviews*, *200*(1), 261–355. https://doi.org/10.1007/s11214-016-0252-5

Artemyev, A., Agapitov, O. V., Mourenas, D., Krasnoselskikh, V., & Zelenyi, L. M. (2013). Storm-induced energization of radiation belt electrons: Effect of wave obliquity: DST dependence of lifetime/energization. *Geophysical Research Letters*, *40*(16), 4138–4143. https://doi.org/10.1002/grl.50837

Bale, S. D., Badman, S. T., Bonnell, J. W., Bowen, T. A., Burgess, D., Case, A. W., et al. (2019). Highly structured slow solar wind emerging from an equatorial coronal hole. *Nature*, *576*(7786), 237–242. https://doi.org/10.1038/s41586-019-1818-7

Bale, S. D., Goetz, K., Harvey, P. R., Turin, P., Bonnell, J. W., Dudok de Wit, T., et al. (2016). The FIELDS instrument suite for solar probe plus: Measuring the coronal plasma and magnetic field, plasma waves and turbulence, and radio signatures of solar transients. *Space Science Reviews*, *204*(1–4), 49–82. https://doi.org/10.1007/s11214-016-0244-5

Bercic, L., Maksimovic, M., Landi, S., & Matteini, L. (2019). Scattering of Strahl electrons in the solar wind between 0.3 and 1 AU: Helios observations. *Monthly Notices of the Royal Astronomical Society*, *486*(3), 3404–3414. https://doi.org/10.1093/mnras/stz1007

Bošková, J., Tříska, P., Omelchenko, Y. A., Shapiro, V. D., & Sotnikov, V. I. (1992). The "fan" instability as a possible generating mechanism of VLF quarter-gyrofrequency emissions during the recovery phase of a magnetospheric storm. *Studia Geophysica et Geodaetica*, *36*(2), 177–187. https://doi.org/10.1007/BF01614129

Breneman, A., Cattell, C., Schreiner, S., Kersten, K., Wilson, L. B., Kellogg, P., et al. (2010). Observations of large-amplitude, narrowband whistlers at stream interaction regions: Large-amplitude whistlers in solar wind. *Journal of Geophysical Research*, *115*(A8), A08104. https://doi.org/10.1029/2009JA014920

Case, A. W., Kasper, J. C., Stevens, M. L., Korreck, K. E., Paulson, K., Daigneau, P., et al. (2020). The solar probe cup on the Parker Solar Probe. *The Astrophysical Journal - Supplement Series*, *246*(2), 43. https://doi.org/10.3847/1538-4365/ab5a7b

Cattell, C., Breneman, A., Dombeck, J., Hanson, E., Johnson, M., Halekas, J., et al. (2022). Parker Solar Probe evidence for the absence of Whistlers close to the Sun to scatter Strahl and to regulate heat flux. *The Astrophysical Journal Letters*, *924*(2), L33. https://doi.org/10.3847/2041-8213/ac4015

Cattell, C., Breneman, A., Dombeck, J., Short, B., Wygant, J., Halekas, J., et al. (2021). Parker Solar Probe evidence for scattering of electrons in the young solar wind by narrowband Whistler-mode waves. *The Astrophysical Journal Letters*, *911*(2), L29. https://doi.org/10.3847/2041-8213/abefdd

Cattell, C., Short, B., Breneman, A. W., & Grul, P. (2020). Narrowband large amplitude whistler-mode waves in the solar wind and their association with electrons: STEREO waveform capture observations. *The Astrophysical Journal*, *897*(2), 126. https://doi.org/10.3847/1538-4357/ab961f

Cattell, C., & Vo, T. (2021). Modeling interactions of narrowband large amplitude whistler-mode waves with electrons in the solar wind inside 0.3 AU and at 1 AU using a particle tracing code. *The Astrophysical Journal Letters*, *914*(2), L33. https://doi.org/10.3847/2041-8213/ac08a1

Chust, T., Kretzschmar, M., Graham, D. B., Le Contel, O., Retinò, A., Alexandrova, A., et al. (2021). Observations of whistler mode waves by solar orbiter's RPW low frequency receiver (LFR): In-flight performance and first results. *Astronomy & Astrophysics*, *656*, A17. https://doi.org/10.1051/0004-6361/202140932

Dudok de Wit, T., Krasnoselskikh, V. V., Agapitov, O., Froment, C., Larosa, A., Bale, S. D., et al. (2022). First results from the SCM search-coil magnetometer on Parker Solar Probe. *Journal of Geophysical Research: Space Physics*, *127*(4), e2021JA030018. https://doi.org/10.1029/2021JA030018

Dudok de Wit, T., Krasnoselskikh, V. V., Bale, S. D., Bonnell, J. W., Bowen, T. A., Chen, C. H. K., et al. (2020). Switchbacks in the near-Sun Magnetic Field: Long memory and impact on the turbulence cascade. *The Astrophysical Journal - Supplement Series*, *246*(2), 39. https://doi.org/10.3847/1538-4365/ab5853

Feldman, W. C., Asbridge, J. R., Bame, S. J., Gosling, J. T., & Lemons, D. S. (1978). Characteristic electron variations across simple high-speed solar wind streams. *Journal of Geophysical Research*, *83*(A11), 5285–5295. https://doi.org/10.1029/JA083iA11p05285

Feldman, W. C., Asbridge, J. R., Bame, S. J., Montgomery, M. D., & Gary, S. P. (1975). Solar wind electrons. *Journal of Geophysical Research*, *80*(31), 4181–4196. https://doi.org/10.1029/JA080i031p04181

Feynman, R. P. (1964). *The Feynman lectures on physics, vol. II: The new millennium edition: Mainly electromagnetism and matter*. Basic Books.

Fox, N. J., Velli, M. C., Bale, S. D., Decker, R., Driesman, A., Howard, R. A., et al. (2016). The Solar Probe plus mission: Humanity's first visit to our star. *Space Science Reviews*, *204*(1–4), 7–48. https://doi.org/10.1007/s11214-015-0211-6

Froment, C., Agapitov, O. V., Krasnoselskikh, V., Karbashewski, S., Dudok De Wit, T., Larosa, A., et al. (2023). Whistler waves generated inside magnetic dips in the young solar wind: Observations of the search-coil magnetometer on board Parker Solar Probe. *Astronomy & Astrophysics*, *672*, A135. https://doi.org/10.1051/0004-6361/202245140

Gary, S. P., & Feldman, W. C. (1977). Solar wind heat flux regulation by the whistler instability. *Journal of Geophysical Research*, *82*(7), 1087–1094. https://doi.org/10.1029/JA082i007p01087

Gary, S. P., Feldman, W. C., Forslund, D. W., & Montgomery, M. D. (1975). Electron heat flux instabilities in the solar wind. *Geophysical Research Letters*, *2*(3), 79–82. https://doi.org/10.1029/GL002i003p00079

Gary, S. P., Skoug, R. M., & Daughton, W. (1999). Electron heat flux constraints in the solar wind. *Physics of Plasmas*, *6*(6), 2607–2612. https://doi.org/10.1063/1.873532

Graham, G. A., Rae, I. J., Owen, C. J., Walsh, A. P., Arridge, C. S., Gilbert, L., et al. (2017). The evolution of solar wind Strahl with heliospheric distance. *Journal of Geophysical Research: Space Physics*, *122*(4), 3858–3874. https://doi.org/10.1002/2016JA023656

Gurnett, D. A., & Anderson, R. R. (1977). Plasma wave electric fields in the solar wind: Initial results from Helios 1. *Journal of Geophysical Research*, *82*(4), 632–650. https://doi.org/10.1029/JA082i004p00632

Halekas, J. S., Whittlesey, P., Larson, D. E., McGinnis, D., Maksimovic, M., Berthomier, M., et al. (2020). Electrons in the young solar wind: First results from the *Parker Solar Probe*. *The Astrophysical Journal - Supplement Series*, *246*(2), 22. https://doi.org/10.3847/1538-4365/ab4cec

Halekas, J. S., Whittlesey, P. L., Larson, D. E., McGinnis, D., Bale, S. D., Berthomier, M., et al. (2021). Electron heat flux in the near-Sun environment. *Astronomy & Astrophysics*, *650*, A15. https://doi.org/10.1051/0004-6361/202039256

Hammond, C. M., Feldman, W. C., McComas, D. J., Phillips, J. L., & Forsyth, R. J. (1996). Variation of electron-strahl width in the high-speed solar wind: ULYSSES observations. *Astronomy and Astrophysics*, *316*, 350–354. Retrieved from https://ui.adsabs.harvard.edu/abs/1996A&A…316..350H/abstract

Howard, R. A., Vourlidas, A., Bothmer, V., Colaninno, R. C., DeForest, C. E., Gallagher, B., et al. (2019). Near-Sun observations of an F-corona decrease and K-corona fine structure. *Nature*, *576*(7786), 232–236. https://doi.org/10.1038/s41586-019-1807-x

Jagarlamudi, V. K., Alexandrova, O., Bercic, L., Dudok de Wit, T., Krasnoselskikh, V., Maksimovic, M., & Stverak, S. (2020). Whistler waves and electron properties in the inner heliosphere: Helios observations. *The Astrophysical Journal*, *897*(2), 118. https://doi.org/10.3847/1538-4357/ab94a1

Jagarlamudi, V. K., Dudok de Wit, T., Froment, C., Krasnoselskikh, V., Larosa, A., Bercic, L., et al. (2021). Whistler wave occurrence and the interaction with strahl electrons during the first encounter of Parker Solar Probe. *Astronomy & Astrophysics*, *650*, A9. https://doi.org/10.1051/0004-6361/202039808

Jannet, G., Dudok de Wit, T., Krasnoselskikh, V., Kretzschmar, M., Fergeau, P., Bergerard-Timofeeva, M., et al. (2021). Measurement of magnetic field fluctuations in the Parker Solar Probe and solar orbiter missions. *Journal of Geophysical Research: Space Physics*, *126*(2), e2020JA028543. https://doi.org/10.1029/2020JA028543

Kadomtsev, B. B., & Pogutse, O. P. (1968). Electric conductivity of a plasma in a strong magnetic field. *Soviet Journal of Experimental and Theoretical Physics*, *26*, 1146. Retrieved from https://ui.adsabs.harvard.edu/abs/1968JETP…26.1146K

Kajdič, P., Alexandrova, O., Maksimovic, M., Lacombe, C., & Fazakerley, A. N. (2016). Suprathermal electron Strahl widths in the presence of narrow-band whistler waves in the solar wind. *The Astrophysical Journal*, *833*(2), 172. https://doi.org/10.3847/1538-4357/833/2/172

Karbashewski, S., Agapitov, O., Kim, H., Mozer, F., Bonnell, J., Froment, C., et al. (2023). Whistler wave observations by Parker Solar Probe during encounter 1: Counter-propagating whistlers collocated with magnetic field inhomogeneities and their application to electric field measurement calibration. *The Astrophysical Journal*, *947*(2), 73. https://doi.org/10.3847/1538-4357/acc527

Kasper, J. C., Abiad, R., Austin, G., Balat-Pichelin, M., Bale, S. D., Belcher, J. W., et al. (2016). Solar wind electrons alphas and protons (SWEAP) investigation: Design of the solar wind and coronal plasma instrument suite for Solar Probe Plus. *Space Science Reviews*, *204*(1), 131–186. https://doi.org/10.1007/s11214-015-0206-3

Kasper, J. C., Bale, S. D., Belcher, J. W., Berthomier, M., Case, A. W., Chandran, B. D. G., et al. (2019). Alfvénic velocity spikes and rotational flows in the near-Sun solar wind. *Nature*, *576*(7786), 228–231. https://doi.org/10.1038/s41586-019-1813-z

Krafft, C., & Volokitin, A. (2003). Interaction of suprathermal solar wind electron fluxes with sheared whistler waves: Fan instability. *Annales Geophysicae*, *21*(7), 1393–1403. https://doi.org/10.5194/angeo-21-1393-2003

Krasnoselskikh, V., Larosa, A., Agapitov, O., Dudok de Wit, T., Moncuquet, M., Mozer, F. S., et al. (2020). Localized magnetic-field structures and their boundaries in the near-sun solar wind from Parker Solar Probe measurements. *The Astrophysical Journal*, *893*(2), 93. https://doi.org/10.3847/1538-4357/ab7f2d

Kretzschmar, M., Chust, T., Krasnoselskikh, V., Graham, D., Colomban, L., Maksimovic, M., et al. (2021). Whistler waves observed by solar orbiter/RPW between 0.5 AU and 1 AU. *Astronomy & Astrophysics*, *656*, A24. https://doi.org/10.1051/0004-6361/202140945

Lacombe, C., Alexandrova, O., Matteini, L., Santolík, O., Cornilleau-Wehrlin, N., Mangeney, A., et al. (2014). Whistler mode waves and the electron heat flux in the solar wind: Cluster observations. *The Astrophysical Journal*, *796*(1), 5. https://doi.org/10.1088/0004-637X/796/1/5

Lazar, M., Pierrard, V., Poedts, S., & Fichtner, H. (2020). Characteristics of solar wind suprathermal halo electrons. *Astronomy & Astrophysics*, *642*, A130. https://doi.org/10.1051/0004-6361/202038830

Lazar, M., Poedts, S., & Michno, M. J. (2013). Electromagnetic electron whistler-cyclotron instability in bi-Kappa distributed plasmas. *Astronomy & Astrophysics*, *554*, A64. https://doi.org/10.1051/0004-6361/201220550

Lazar, M., Poedts, S., & Schlickeiser, R. (2011). Instability of the parallel electromagnetic modes in Kappa distributed plasmas—I. Electron whistler-cyclotron modes: Stability of Kappa distributed plasmas—I. *Monthly Notices of the Royal Astronomical Society*, *410*(1), 663–670. https://doi.org/10.1111/j.1365-2966.2010.17472.x

Lazar, M., Poedts, S., Schlickeiser, R., & Dumitrache, C. (2015). Towards realistic parametrization of the kinetic anisotropy and the resulting instabilities in space plasmas. Electromagnetic electron–cyclotron instability in the solar wind. *Monthly Notices of the Royal Astronomical Society*, *446*(3), 3022–3033. https://doi.org/10.1093/mnras/stu2312

Lazar, M., Yoon, P. H., López, R. A., & Moya, P. S. (2018). Electromagnetic electron cyclotron instability in the solar wind. *Journal of Geophysical Research: Space Physics*, *123*(1), 6–19. https://doi.org/10.1002/2017JA024759

López, R. A., Shaaban, S. M., Lazar, M., Poedts, S., Yoon, P. H., Micera, A., & Lapenta, G. (2019). Particle-in-cell simulations of the whistler heat-flux instability in solar wind conditions. *The Astrophysical Journal*, *882*(1), L8. https://doi.org/10.3847/2041-8213/ab398b

Maksimovic, M., Pierrard, V., & Lemaire, J. F. (1997). A kinetic model of the solar wind with Kappa distribution functions in the corona. *Astronomy and Astrophysics*, *324*, 725–734. Retrieved from https://ui.adsabs.harvard.edu/abs/1997A&A…324..725M

Maksimovic, M., Zouganelis, I., Chaufray, J.-Y., Issautier, K., Scime, E. E., Littleton, J. E., et al. (2005). Radial evolution of the electron distribution functions in the fast solar wind between 0.3 and 1.5 AU. *Journal of Geophysical Research*, *110*(A9), A09104. https://doi.org/10.1029/2005JA011119

Malaspina, D. M., Ergun, R. E., Bolton, M., Kien, M., Summers, D., Stevens, K., et al. (2016). The digital fields board for the FIELDS instrument suite on the Solar Probe plus mission: Analog and digital signal processing. *Journal of Geophysical Research: Space Physics*, *121*(6), 5088–5096. https://doi.org/10.1002/2016JA022344

McComas, D., Christian, E., Cohen, C., Cummings, A., Davis, A., Desai, M., et al. (2019). Probing the energetic particle environment near the Sun. *Nature*, *576*(7786), 223–227. https://doi.org/10.1038/s41586-019-1811-1

Means, J. D. (1972). Use of the three-dimensional covariance matrix in analyzing the polarization properties of plane waves. *Journal of Geophysical Research*, *77*(28), 5551–5559. https://doi.org/10.1029/JA077i028p05551

Micera, A., Zhukov, A. N., López, R. A., Boella, E., Tenerani, A., Velli, M., et al. (2021). On the role of solar wind expansion as a source of whistler waves: Scattering of suprathermal electrons and heat flux regulation in the inner heliosphere. *The Astrophysical Journal*, *919*(1), 42. https://doi.org/10.3847/1538-4357/ac1067

Micera, A., Zhukov, A. N., López, R. A., Innocenti, M. E., Lazar, M., Boella, E., & Lapenta, G. (2020). Particle-In-Cell simulation of Whistler heat flux instabilities in the solar wind: Heat flux regulation and electron halo formation. *The Astrophysical Journal Letters*, *903*(1), L23. https://doi.org/10.3847/2041-8213/abc0e8

Neubauer, F. M., Musmann, G., & Dehmel, G. (1977). Fast magnetic fluctuations in the solar wind: Helios 1. *Journal of Geophysical Research*, *82*(22), 3201–3212. https://doi.org/10.1029/JA082i022p03201

Paschmann, G., & Daly, P. W. (1998). Analysis methods for multi-spacecraft data. ISSI scientific reports Series SR-001. In *ISSI scientific reports series, 1* (Vol. 1). ESA/ISSI. Retrieved from https://ui.adsabs.harvard.edu/abs/1998ISSIR…1…..P

Pilipp, W. G., Miggenrieder, H., Montgomery, M. D., Mühlhäuser, K. H., Rosenbauer, H., & Schwenn, R. (1987). Characteristics of electron velocity distribution functions in the solar wind derived from the Helios plasma experiment. *Journal of Geophysical Research*, *92*(A2), 1075–1092. https://doi.org/10.1029/JA092iA02p01075

Raouafi, N. E., Matteini, L., Squire, J., Badman, S. T., Velli, M., Klein, K. G., et al. (2023). Parker Solar probe: Four years of discoveries at solar cycle minimum. arXiv. 10.48550/arXiv.2301.02727.

Roberg-Clark, G. T., Agapitov, O., Drake, J. F., & Swisdak, M. (2019). Scattering of energetic electrons by heat-flux-driven Whistlers in flares. *The Astrophysical Journal*, *887*(2), 190. https://doi.org/10.3847/1538-4357/ab5114

Rosenbauer, H., Miggenrieder, H., Montgomery, M., & Schwenn, R. (1976). Preliminary results of the Helios plasma measurements. In *Physics of solar planetary environments: Proceedings of the international symposium on solar—Terrestrial physics, June 7–18,1976 Boulder, Colorado, volume I* (pp. 319–331). American Geophysical Union (AGU). https://doi.org/10.1029/SP007p0319

Rosenbauer, H., Schwenn, R., Marsch, E., Meyer, B., Miggenrieder, H., Montgomery, M. D., et al. (1977). A survey on initial results of the HELIOS plasma experiment. *Journal of Geophysics Zeitschrift Geophysik*, *42*, 561–580. Retrieved from https://ui.adsabs.harvard.edu/abs/1977JGZG…42..561R

Sagdeev, R. Z., & Shafranov, V. D. (1960). On the instability of a plasma with an anisotropic distribution of velocities in a magnetic field. *Zhur. Eksptl'. i Teoret. Fiz.*, *39*. Retrieved from https://www.osti.gov/biblio/4135931

Saito, S., & Gary, S. P. (2007). All whistlers are not created equally: Scattering of strahl electrons in the solar wind via particle-in-cell simulations. *Geophysical Research Letters*, *34*(1), L01102. https://doi.org/10.1029/2006GL028173

Santolík, O., Parrot, M., & Lefeuvre, F. (2003). Singular value decomposition methods for wave propagation analysis: SVD methods for wave propagation analysis. *Radio Science*, *38*(1). https://doi.org/10.1029/2000RS002523

Sarfraz, M., & Yoon, P. H. (2020). Combined Whistler heat flux and anisotropy instabilities in solar wind. *Journal of Geophysical Research: Space Physics*, *125*(1), e2019JA027380. https://doi.org/10.1029/2019JA027380

Scime, E. E., Bame, S. J., Feldman, W. C., Gary, S. P., Phillips, J. L., & Balogh, A. (1994). Regulation of the solar wind electron heat flux from 1 to 5 AU: Ulysses observations. *Journal of Geophysical Research*, *99*(A12), 23401–23410. https://doi.org/10.1029/94JA02068

Scudder, J. D. (1992a). On the causes of temperature change in inhomogeneous low-density astrophysical plasmas. *The Astrophysical Journal*, *398*, 299. https://doi.org/10.1086/171858

Scudder, J. D. (1992b). Why all stars should possess circumstellar temperature inversions. *The Astrophysical Journal*, *398*, 319. https://doi.org/10.1086/171859

Sonnerup, B. U., & Cahill, L. J., Jr. (1967). Magnetopause structure and attitude from Explorer 12 observations. *Journal of Geophysical Research*, *72*(1), 171–183. https://doi.org/10.1029/JZ072i001p00171

Sonnerup, B. U., & Scheible, M. (1998). Minimum and maximum variance analysis. *ISSI Scientific Reports Series*, *1*, 185–220. Retrieved from https://ui.adsabs.harvard.edu/abs/1998ISSIR…1..185S

Stansby, D., Horbury, T. S., Chen, C. H. K., & Matteini, L. (2016). Experimental determination of Whistler wave dispersion relation in the solar wind. *The Astrophysical Journal*, *829*(1), L16. https://doi.org/10.3847/2041-8205/829/1/L16

Štverák, t., Maksimovic, M., Trávníček, P. M., Marsch, E., Fazakerley, A. N., & Scime, E. E. (2009). Radial evolution of nonthermal electron populations in the low-latitude solar wind: Helios, Cluster, and Ulysses Observations. *Journal of Geophysical Research*, *114*(A5), A05104. https://doi.org/10.1029/2008JA013883

Taubenschuss, U., & Santolík, O. (2019). Wave polarization analyzed by singular value decomposition of the spectral matrix in the presence of noise. *Surveys in Geophysics*, *40*(1), 39–69. https://doi.org/10.1007/s10712-018-9496-9

Tong, Y., Vasko, I., Artemyev, A., Bale, S., & Mozer, F. (2019). Statistical study of Whistler waves in the solar wind at 1 AU. *The Astrophysical Journal*, *878*, 41. https://doi.org/10.3847/1538-4357/ab1f05

Tong, Y., Vasko, I. Y., Pulupa, M., Mozer, F. S., Bale, S. D., Artemyev, A. V., & Krasnoselskikh, V. (2019). Whistler wave generation by Halo electrons in the solar wind. *The Astrophysical Journal*, *870*(1), L6. https://doi.org/10.3847/2041-8213/aaf734

Vasko, I. Y., Krasnoselskikh, V., Tong, Y., Bale, S. D., Bonnell, J. W., & Mozer, F. S. (2019). Whistler fan instability driven by strahl electrons in the solar wind. *The Astrophysical Journal*, *871*(2), L29. https://doi.org/10.3847/2041-8213/ab01bd

Vasko, I. Y., Kuzichev, I. V., Artemyev, A. V., Bale, S. D., Bonnell, J. W., & Mozer, F. S. (2020). On quasi-parallel whistler waves in the solar wind. *Physics of Plasmas*, *27*(8), 082902. https://doi.org/10.1063/5.0003401

Verscharen, D., Chandran, B. D. G., Jeong, S.-Y., Salem, C. S., Pulupa, M. P., & Bale, S. D. (2019). Self-induced scattering of strahl electrons in the solar wind. *The Astrophysical Journal*, *886*(2), 136. https://doi.org/10.3847/1538-4357/ab4c30

Vocks, C., & Mann, G. (2003). Generation of suprathermal electrons by resonant wave-particle interaction in the solar corona and wind. *The Astrophysical Journal*, *593*(2), 1134–1145. https://doi.org/10.1086/376682

Vocks, C., Salem, C., Lin, R. P., & Mann, G. (2005). Electron Halo and strahl formation in the solar wind by resonant interaction with Whistler waves. *The Astrophysical Journal*, *627*(1), 540–549. https://doi.org/10.1086/430119